IMPROVEMENTS ON PERFORMANCE OF A HEAT PUMP WATER HEATER SYSTEM

BY

CE SHI

THESIS

Submitted in partial fulfillment of the requirements
for the degree of Master of Science in Mechanical Engineering
in the Graduate College of the
University of Illinois at Urbana-Champaign, 2018

Urbana, Illinois

Adviser:

Professor Predrag S. Hrnjak

ABSTRACT

Heat Pump Water Heater (HPWH) is classified as one renewable energy efficient technology, which could be explained by their environmentally friendly nature with low energy consumption. The Coefficient of Performance (COP) of the HPWH can be influenced by multiple factors: ambient temperature, relative humidity, hot water usage profile, the size and shape of heat exchangers (evaporator and condenser), type and shape of compressor, refrigerant, filling capacity of refrigerant, etc. Therefore, in this study, the performance of HPWH is critically examine to ascertain its optimal operation condition. Three main factors are considered here: use pattern of water in tank, drop-in refrigerant R1234yf and condenser configuration. This study examines two different models, HPWH-66 and HPWH-50. Simulation is employed and suggestions are made towards a better performance. The performance of HPWH system is found to strongly depend on the stratification of water in the storage tank, then 3D CFD simulation has been used to explore the entrance effects on the thermal tank. In the drop-in experiments, it is shown that R1234yf can be a desirable alternative for the baseline R134a without any special changes to the heat pump facility. By closing the valves at the inlet and outlet of one condenser circuit, a one-circuit condenser system could be achieved. For both refrigerant system, one-circuit condenser only brings the COP down within 5.5%. Finally, a linked EES-Fluent model has been developed to simulate the transient heating-up performance of the HPWH system with the validation by experimental data.

ACKNOWLEDGEMENTS

This research project was funded by the Air Conditioning and Refrigeration Center (ACRC) in University of Illinois at Urbana-Champaign. Foremost, I would like to deliver my most sincere gratitude to my advisor Prof. Pega Hrnjak for his continuous support, encouragement, as well as the professional academic guidelines, he has taught more than I could ever give him the credit here. Special appreciation goes to the A.O Smith for providing the heat pump water heater unit and lots of valuable advice. I am grateful to all the colleagues who I had the pleasure to work with and assisted me at every point to cherish my goal.

Finally, I must express my most profound gratitude to my parents, whose love and encouragement are with me in whatever I pursue. Without their unfailing support, this paper would not be accomplished.

TABLE OF CONTENTS

LIST OF FIGURES

LIST OF TABLES

NOMENCLATURE

A	Area, m^2
C	Heat capacity rate, KJ $s^{-1}K^{-1}$
C_r	Heat capacity ratio
COP	Coefficient of performance
D	Diameter, m
D_h	Hydraulic diameter, m
D_c	Collar diameter, m
EES	Engineering Equation Solver
EEV	Electronic Expansion Valve
f	Friction factor
F_p	Fin pitch, m
F_r	Froude number
g	Gravitational acceleration, m s^{-2}
G	Mass flux, kg m^{-2} s^{-1}
h	Enthalpy, kg kJ^{-1} or heat transfer coefficient, W m^{-2} K
k	Conductivity, W m^{-1} K^{-1}
L	Length, m
$\dot{m}$	Mass flow rate, g s^{-1}
M	Mass, kg
NTU	Number of Transfer Unit
Nu	Nusselt number

PID	Proportional Integral Derivative
POE	Polyol ester oil
P	Pressure, kPa
Pr	Prandtl number
Q	Heat exchanger capacity, kW
Re	Reynolds number
Ri	Richardson number
t	time, s
T	Temperature, ℃ or K
u	Velocity, m s^{-1} or uncertainty
U	Overall uncertainty
V	Volume, m^3
$\dot{V}$	Volumetric flow rate, m^3 s^{-1}
Vol	Element volume, m^3
W	Work or power, kW
x	vapor quality
X_{tt}	Lockhart-Martinelli number

Greek Symbols

α	Void fraction
δ	Thickness, m
ε	Effectiveness or surface roughness, m
η	Efficiency

μ	Dynamic viscosity, Pa s^{-1}
ρ	Density, kg m^{-3}
σ	Surface tension, N m^{-1}
ϕ	Two-phase multiplier
ω	Refrigerant mass fraction

Subscripts

Comp	Compressor
cond or c	Condenser
evap or e	Evaporator
i	Layer or inlet
in	Inlet
str	Stratified
mix	Mixed
out or o	Outlet
r	Refrigerant
sys	System
vap or v	Vapor

CHAPTER 1-INTRODUCTION

1.1 Overview

Heat pump water heaters (HPWHs) are increasingly used for residential heating applications. They offer higher efficiency than conventional electric resistance water heaters and reduce the energy consumption. Therefore, HPWH is a more environmentally friendly surrogate for residential heating.

Numerous research has been conducted on the performance of HPWHs with various complex parameters, such as the working fluid, tank size, water draw flow rate, heat exchangers, and etc. Various analysis approach have been developed, such as the entropy generation, exergy loss and energy analysis, for individual components as well as the whole HPWH system.

One of the questions is to find a good design on the tank side that would provide good efficiency at various user patterns (different amounts of water or different water flow rates). After certain amount of hot water has been used and replaced with cold water at a certain flow rate, it is of interest to investigate how much electricity is needed to bring the water temperature in the tank back to the temperature before consumption and how the water usage amount and the draw rate affect the energy efficiency.

Another significant parameter is the refrigerant used in the vapor compression cycle. R134a has been chosen as the most current HPWH working fluid due to its relatively high Unified Energy Factor (UEF). However, with the increasing concern with respect to its high Global Warming Potential (GWP), R134a has been discouraged in the use of HPWH applications. Therefore, finding promising low-GWP alternative refrigerants for HPWHs becomes important. Among the low-GWP alternatives, R1234yf has been universally considered as a possible drop-in replacement for R134a in HPWH applications due to its zero Ozone depletion potential (ODP)

and promising life-cycle climate performance. Furthermore, its thermodynamic properties and heat transfer coefficient are quite similar to those of R134a (the boiling temperature is only 3.7℃ lower than that of R134a).

In order to improve the system performance and decrease the product expense, the system components need to be explored. Some hardware modifications can be done regarding the tube size and tube length of the heat exchangers, which results in a change of the refrigerant charge quantity. It is important for a system to obtain the optimized refrigerant filling quantity. If the charge is too much, the compressor load will be aggravated and the odd refrigerant will occupy the condenser area which results in the efficiency decrease; on the other hand, insufficient charge will cause lower discharge pressure in compressor, which lowers the heating capacity. Therefore, by matching up the proper filling quantity and the heat exchanger size, the product cost can be reduced.

Finally, a system model should be developed to predict the heating-up performance for the HPWH system, and validated by the experimental data.

1.2 Literature Review

1.2.1 Review on the effect of use pattern on HPWH performance

Jordan and Furbo [1] found that the draw-offs and charging period can significantly influence the thermal stratification and system efficiency of storage tanks. To enhance the thermal stratification, various entrance designs were proposed by the authors. Yee and Lai [2] investigated the effect of a porous material in the storage tank on stratification. Dragsted et al. [3] presented that the inlet stratifiers could tremendously help to assign the stratification.

It is important to determine an index to characterize the ability for a thermal water tank to maintain and promote stratification during the draw period. Quantification of mixing is a

complicated task and has been investigated in many literatures. Davidson et al. [4] used MIX number to determine water mixing on energy level. Rosen et al. [5] proposed that the mixing of fluids with different temperatures always led to entropy generation and exergy loss. Haller et al. [6] presented a new method to calculate the stratification efficiency based on the second law of thermodynamics. They studied the effect of heat loss on stratification efficiency by using the relative entropy/exergy loss approach. Castell et al. [7] used the Richardson number to describe the thermal stratification in the storage tank.

1.2.2 Review on the drop-in replacement R1234yf

There have been numerous researches about the R1234yf as a drop-in alternative of R134a in the vapor compression systems. Lee and Jung [8] compared the performance of R134a and R1234yf, and concluded that there were only tiny difference in capacities while the compressor discharge temperature reduced by 6°F. Zilio [9] et al. investigated the experimental research using R1234yf as the drop-in to compare with a R134a baseline mobile air conditioning (MAC) system. Mota-Babiloni et al. [10] and Navarro-Esbrí [11] compared with energy performance of vapor compression systems with R134a and R1234yf. By controlling the condensing and evaporating temperature, it is shown that the cooling capacity and COP of the R1234yf system decreased by 9% and 13%, respectively, while the volumetric efficiency was approximately 5% lower than that of R134a. Cho et al. [12] investigated the experiments in a MAC system, with a focus on performance of R134a and R1234yf with and without an internal heat exchanger. It was shown that compared with R134a, the cooling capacity and COP of R1234yf decreased by up to 7%, while those with the internal heat exchanger decreased by up to 2.9%. Lee et al. [13] conducted experiments to compare a heat pump bench performance using R134a and R134a/R1234yf (10/90%) mixture. It showed that the COP and capacities using R134a/R1234yf is quite similar

to that of R134a. It can be concluded from these researches that the COP and capacity of R1234yf are close to those of R134a.

1.2.3 Review on modelling of thermal component and system

Even though most of the research focuses on the experiments, there are still several studies using the numerical ways to describe the thermal performance of a heat exchanger or a system. The most common method is still one-dimensional modeling based on correlations [14]. Baeten et al. [15] developed a one-dimensional model using the data from experiments and CFD simulations as the model parameters, and investigated the buoyancy effect as well as the mixing principles. Fan et al. [16] explored a solar thermal tank with a heat exchanger spiral inside. They studied the effect of natural convection on thermal stratification as well as the factors that influenced the stratification pattern. Then, they came up with a correlation that considered the effects of volume, thickness, material, aspect ratio and initial conditions of the tank.

It is challengeable to model a HPWH system due to the complexity to integrate the model of the thermal tank with that of the vapor compression cycle. Only several studies have considered the details for an integrated system, such as the wrapped around coil condenser configuration, thermal stratification, tank heat loss and etc. Shah and Hrnjak [17] proposed a linked model to integrate both water tank and the heat pump system. They developed a steady-state vapor compression system model using Engineering Equation Solver (EES) as well as a CFD tank model in Fluent to describe the quasi-steady heating-up process of a HPWH system. Li and Hrnjak [18] then extended their work and proposed a model for a residential HPWH unit. By exchanging the information through the interface between tank wall and nearby water, their linked model was capable of capturing the transient thermal and dynamic process in the tank, as well as the heat transfer in the vapor compression cycle.

1.3 Research Objective

The primary objective of this study is to explore the improvements of performance in a residential heat pump water heater system. Emphasis goes to three main sections: 1). Experiments have been done to investigate the effect of use pattern on the efficiency of a HPWH unit. Different analysis methods including the Richardson number and Entropy generation are carried out. Then, inspired by the experimental results, CFD simulations are conducted; 2). The potential of R1234yf is accessed to be a drop-in alternative for a R134a baseline HPWH system. The experiments are conducted to determine how much variation occurs between the same system design with R1234yf and R134a, in terms of the refrigerant charge, the capacities, power consumption, COP, etc. 3). One hardware modification has been made on the condenser circuit. After placing four valves at the inlet and outlet of each condenser circuit, one circuit can be shut by closing two ball valves in that circuit. Then experiments are conducted to compare the difference between the two different condenser configurations. Finally, an EES-Fluent linked model is developed to predict the heating-up performance of the HPWH system numerically.

CHAPTER 2 – EXPERIMENTAL SYSTEM

2.1 Experimental facility

Figure 2.1 and 2.2 are the schematic drawing of the HPWH system and the experimental setup. It is a modified facility from Li and Hrnjak [18]. The experimental facility is instrumented on the base of a residential heat pump water heater unit, which contains an evaporator, a low-pressure side accumulator, a back pressure reciprocating compressor, an electronic expansion valve, a wrap-around coil condenser, and a water tank. R134a was initially chosen as the refrigerant and POE 22 is used for the compressor. The condenser has two parallel aluminum coil tubes which are wrapped around the stainless-steel tank wall. The capacity of the water tank is 250 liters (66 gallons).

Figure 2.3 shows the original design for this HPWH containing two immersed electric resistance heating elements to operate instead of using heat pump when being demanded or the temperature difference exceeds the ability of the heat pump to supply hot water. For research purpose, the heating elements have been removed, so that the water heating process only depends on the vapor-compression cycle.

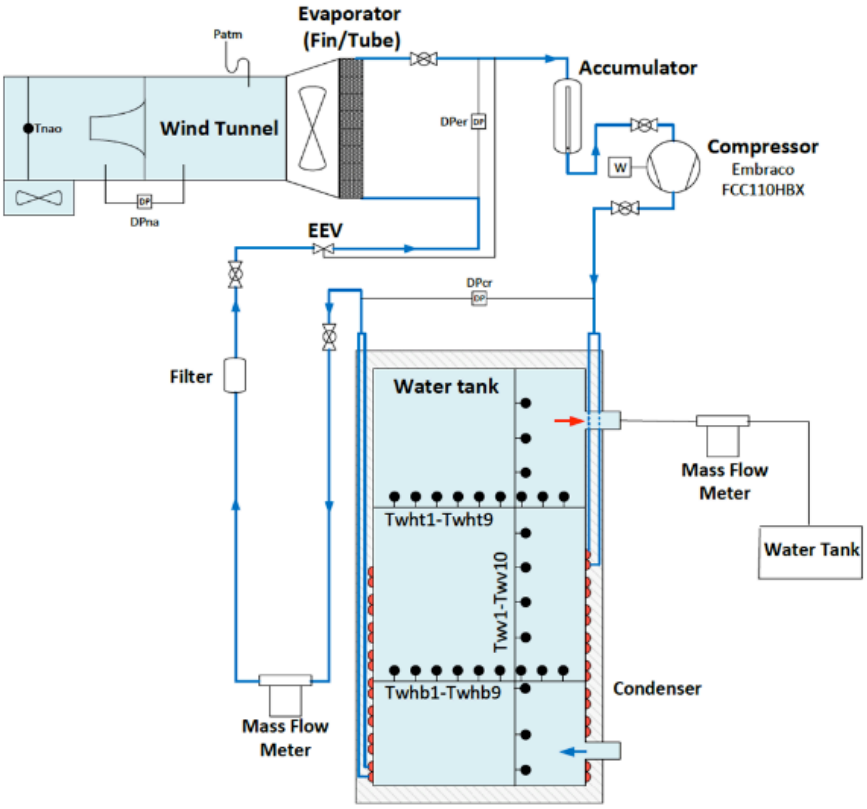

Figure 2.1 Schematic drawing of the HPWH system

Figure 2.2 Experimental Setup

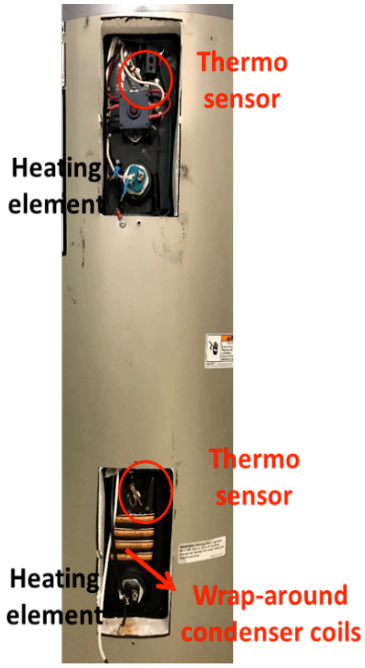

Figure 2.3 Thermo sensors and heating elements in the HPWH

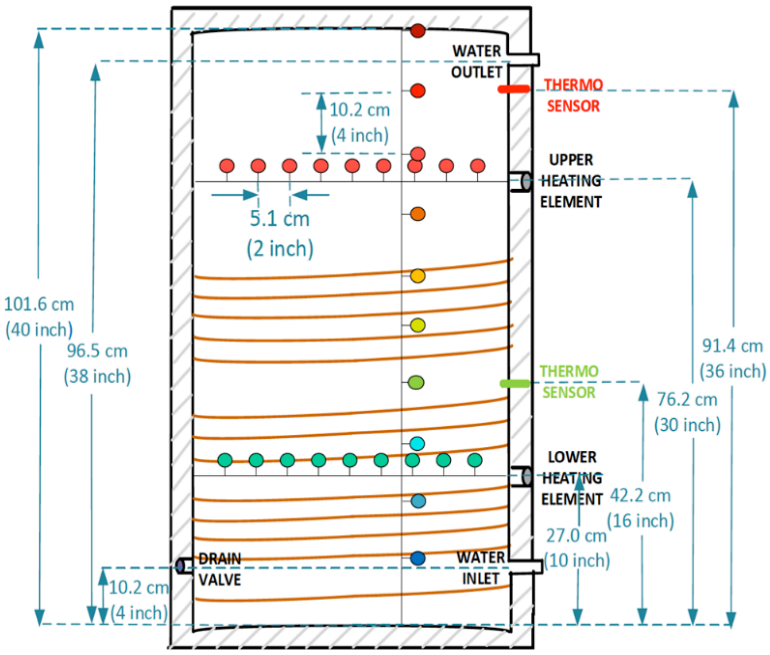

Figure 2.4 Locations of various elements

In order to measure and monitor the temperature and pressure change in the refrigerant loop, T-type immersed thermocouples, absolute and differential pressure transducers have been installed at several significant locations in each components. A Coriolis mass flow meter is placed in the liquid line so that the refrigerant mass flow rate could be measured when the fluid is in subcooling state. A wattmeter is installed to measure the compressor work.

It should be noted that the length of the liquid line in the original HPWH unit is shorter than its current length. That is because the liquid line has been lengthened to accommodate the space to install the mass flow meter.

On the water side, 28 thermocouples are installed inside the storage tank to record the temperature change during the operation, as it shown in Figure 2.4. Ten of them are placed

vertically with 10.16 cm interval, rest are installed horizontally at 27 cm and 76 cm above the tank bottom with 5.08 cm interval.

On the air side, Four Type-T welded thermocouples are mounted on the front surface of the evaporator and one thermocouple is placed at the end of wind tunnel so that the air side temperature change could be monitored. A nozzle is placed inside the wind tunnel so that the air flow velocity can be obtained by the differential pressure transducer in the nozzle. Since the nozzle brings the extra flow resistance, a blower is installed in the wind tunnel so that the resistance can be eliminated. The atmospheric pressure on the back of evaporator can be maintained by adjusting the opening of the wind tunnel.

In order to satisfy the air side energy balance, an environmental chamber where a PID-controlled heater is used to maintain the ambient conditions and provide the heat to the HPWH system.

A 21X Micrologger Datalogger and two multiplexers are used as the data acquisition system. By using an Excel-EES linked processing model, the data can be processed with 0.5 min time interval.

2.2 Data Reduction and Uncertainty

The overall uncertainty for measurements is estimated by the error propagation rule:

$$\mathrm{u} = \sqrt{\sum_{I=1}^{N} \left(\frac{\partial y}{\partial x_i}\right)^2 u^2(x_i)} \tag{2.1}$$

$$\mathrm{Y} = \mathrm{y} \pm \mathrm{U} \tag{2.2}$$

$$\mathrm{U} = 2 \cdot u_c \tag{2.3}$$

Where, y is the calculated variable, x_i is the measured variable and $u(x_i)$ is the uncertainty of the measured variable.

For the Type-T welded and immersed thermocouples which monitor the air/water and refrigerant temperature, respectively, the accuracy for calibration is 0.1℃, the temperature ranges from -200℃ to +200℃.

Absolute pressure transducers are placed at condenser outlet, evaporator inlet and electronic expansion valve inlet. The range is from 0 to 3500 kPa, with an accuracy ±0.25% full scale for condenser outlet, ±0.1% full scale for evaporator inlet, ±0.05% full scale for EEV inlet.

Differential pressure transducers are used for recording the pressure difference for condenser, evaporator and nozzle (in the wind tunnel). The range is from 0 to 103.4 kPa with accuracy ±0.1% full scale for both condenser and evaporator, and for the nozzle, ranges from 0 to 622.7 Pa with ±0.073% full scale.

The refrigerant mass flow rate is monitored by the micro motion mass flowmeter, the range of which is 0- 29.19 g/s with an accuracy of ±0.15% of full scale.

Compressor power and overall power input are measured by wattmeters, ranging from 0-4 kW and 0-1000 kW.

CHAPTER 3 – EXPERIMENT ON WATER SIDE

3.1 Experimental Procedures

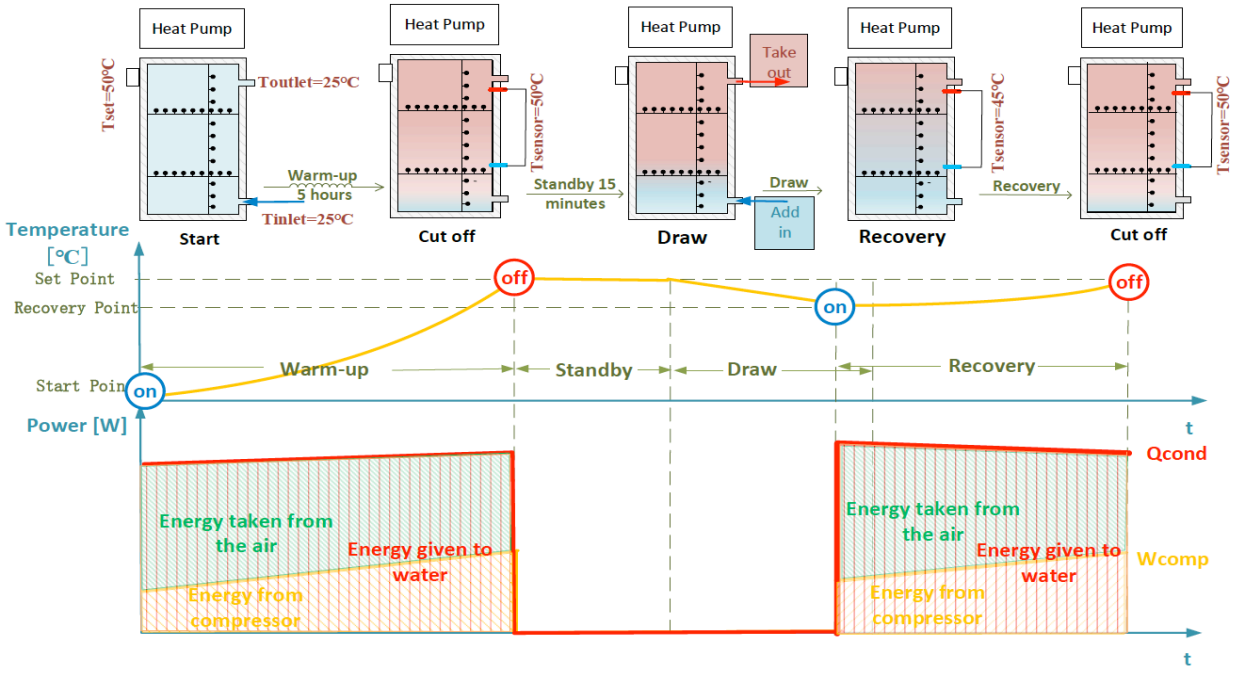

Figure 3.1 Experimental procedures

Figures 3.1 shows the experimental procedures. First, the tank is filled with cold water at 25 ºC, set the set-point at 50 ºC. Then, the heat pump runs until it is cut off automatically. A 15-minute standby period is followed by a given water draw with constant draw rate, at the same time, the tank is refilled with cold water to keep tank full at all time. During the draw period, when the sensor temperature decreases to the recovery point, the heat pump will be automatically restarted by its controller, the system will heat up until it reaches to the set point and will shut off again. The bottom two charts in Figure 3.1 show a schematic drawing prediction of the operation. The ON and OFF represent the condition of heat pump, and the energy given to the water which is the Qcond should be equal to the sum of energy taken from the air and compressor energy.

As Table 3.1 indicates, a series of experiments have been done to investigate the effects of draw amount and draw rate on the performance of the HPWH system.

Four different draw rates were used to test the impact of draw rate on performance: 25 g/s (0.4 gpm), 63 g/s (1 gpm), 126 g/s (2 gpm) and 189 g/s (3 gpm). The other parameters and conditions stayed as constants during the experiments.

Then, five tests were performed under different draw amounts to compare: 57 liter, 144 liter, 152 liter, 190 liter and 250 liter. The other parameters and conditions stay constant during the experiment.

Table 3.1 Experiment conditions on the effect of draw amount and draw rate

<table>
<tr><th>Test #</th><th>Draw amount [liter]</th><th>Draw rate [g/s]</th><th>Draw amount [gallon]</th><th>Draw rate [gallon/min]</th></tr>
<tr><td>1</td><td rowspan="4">152</td><td>25</td><td rowspan="4">40</td><td>0.4</td></tr>
<tr><td>2</td><td>63</td><td>1</td></tr>
<tr><td>3</td><td>126</td><td>2</td></tr>
<tr><td>4</td><td>189</td><td>3</td></tr>
<tr><td colspan="5"></td></tr>
<tr><td>5</td><td>250</td><td rowspan="5">126</td><td>66</td><td rowspan="5">2</td></tr>
<tr><td>6</td><td>190</td><td>50</td></tr>
<tr><td>3</td><td>152</td><td>40</td></tr>
<tr><td>7</td><td>114</td><td>30</td></tr>
<tr><td>8</td><td>57</td><td>15</td></tr>
</table>

3.2 Methods for Characterizing Tank Mixing

The stream of cold water entering the hot storage tank through the inlet port causes turbulent mixing and entrainment of surrounding region close to the tank entrance, even when the water is being charged at a relatively low velocity.

3.2.1 Entropy generation and exergy loss

Mixing with different temperatures always results in entropy generation and exergy loss [19]. When storage tank is maintaining better stratification, less entropy and exergy loss is generated [19]. Therefore, entropy generation and exergy loss have been conducted here to characterize the "usefulness" of the energy stored in the tank. The specific exergy can be quantified according to the Equation (3.1)~(3.4). And the values for each of the ten thermocouples were summed up to represent the exergy stored in the tank.

$$s_i = \frac{Q}{T_i} \tag{3.1}$$

$$s_{tank} = \sum_{i=1}^{n} s_i \tag{3.2}$$

$$E_{xi} = (h_i\text{-}h_0)\text{-}T_0\,(s_i\text{-}s_0) \tag{3.3}$$

$$E_{x\,tank} = \sum_{i=1}^{n} E_{xi} \tag{3.4}$$

Where h_0, s_0, T_0 represents the enthalpy, entropy and temperature at dead sate when the system is in thermodynamic equilibrium.

3.2.2 Richardson number and mixing coefficient

Mixing causes the loss of capacities during the draw period. The degree of mixing depends on the inlet velocity, temperature difference between the cold and hot water and the location of the inlet jet.

The mixing coefficient Z is used to represent the ratio of the sum of the heat capacities of the mixing region and inlet stream mixing with it to the heat capacity of the mixing region.

$$\mathrm{Z} = \frac{Q_{mix}+Q_{inlet\ stream}}{Q_{mix}} \tag{3.5}$$

According to Nelson [20], a correlation is obtained for mixing coefficient Z in terms of $\frac{Re}{Ri}$, to express two dimensionless numbers, Richardson and Reynolds number, which accounts for all the parameters that contributing to the generation of mixing, such as aspect ratio D/L, inlet jet velocity *v*, temperature difference between the initial tank and inlet fluid, etc.

$$Z = 1.688\times10^{4}(\frac{Re}{Ri})^{0.67} \tag{3.6}$$

$$Ri = \frac{g\beta(T_{initial}\text{-}T_{inlet})L}{v^2} \tag{3.7}$$

$$Re = \frac{Dv\rho}{\mu} \tag{3.8}$$

Where, Ri is the convection Richardson number that is calculated from the temperatures, *v* is the bulk flow velocity and Re is the Reynolds number which is based on the average velocity of the flow.

A higher mixing coefficient indicates greater mixing in the thermal storage tank [20].

3.3 Methods for Evaluating System Recovery Performance

In order to evaluate the recovery performance, two definitions are introduced here. Industry defined "Recovery Efficiency" to evaluate the recovery performance from the water side.

$$\eta_{recovery} = \frac{Energy\ in\ the\ water\ delivered\ at\ outlet}{Electricity\ input\ to\ HPWH\ system} = \frac{M_{draw}C_{p,r}(\overline{T}_{out}\text{-}\overline{T}_{in})}{W_{comp}+W_{auxiliary}} \tag{3.9}$$

To calculate the energy delivered at water outlet, M is the mass of the volume drawn and delta T is the average temperature difference between the outlet and inlet during the draw.

The electricity input to HPWH system the overall input work to the water heater from the start of the draw to the recovery end.

At the same time, COP_{system} is defined as the ratio of condensing capacity and electricity input to HPWH system.

$$COP_{system} = \frac{Condensing\ capacity}{Electricity\ input\ to\ HPWH\ system} = \frac{Q_{cond}}{W_{comp} + W_{auxiliary}} \quad (3.10)$$

Therefore, the refrigerant side performance could be investigated and examined whether the twi evaluation remain the same or have other relationships.

CHAPTER 4 – EXPERIMENTAL RESULTS ON WATER SIDE

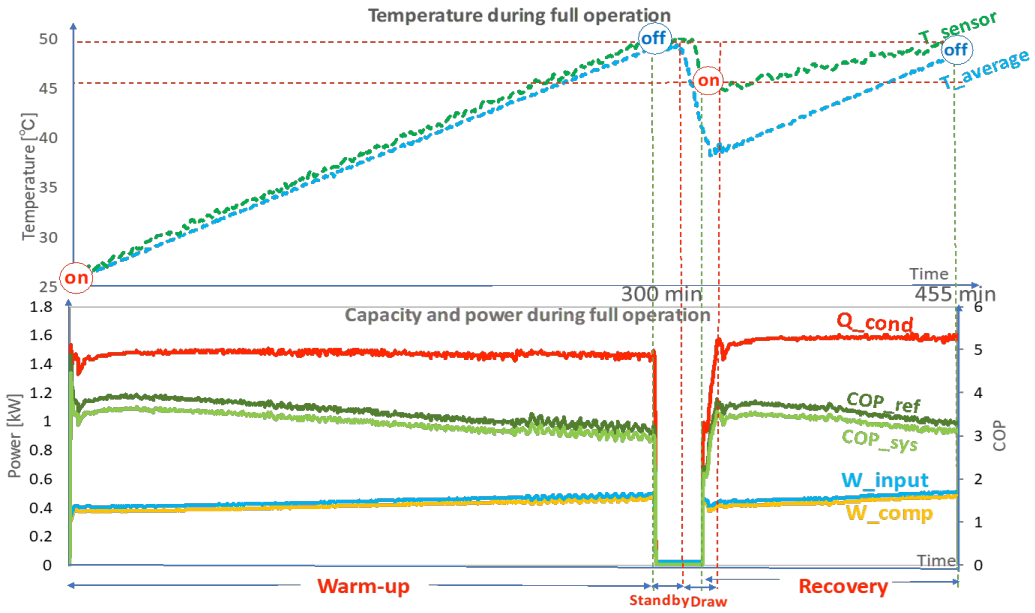

Figure 4.1 Full operation measured at 152 liter, 2gpm

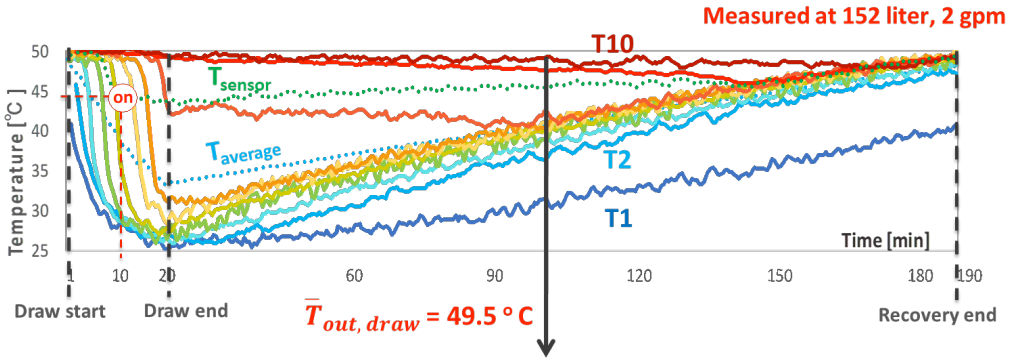

Figure 4.2 Vertical temperature change during recovery period, measured at 152 l, 126 g/s

Figure 4.2 shows the vertical temperature change during recovery period, measured at 152 l, 126 g/s (2 gpm). We measured the temperature on equally vertical interval from the draw start to the recovery end. The gradient color from blue to red represents 10 vertical thermocouples mounted from bottom to the top in the tank.

The temperature difference among each vertical interval indicates the stratification. The wrapped around tank condenser design allows for efficient heat transfer between the refrigerant system and water, this helps maintain tank stratification since the cold inlet water stays at the bottom of the tank and hot water is drawn from the top of the tank. This stratification results in a higher sustained outlet water temperature.

4.1 Effect of Draw Amount on HPWH Performance

The water level for each of five draw amounts changes from 57 liters to 250 liters are shown in Figure 4.3.

Meanwhile, $T_{bottom\ tank}$ is defined as the arithmetic average temperature from T1 to T5, which indicates the water temperature that inside the wrapped around coil condenser area, and since the condensing temperature relies on the water temperature, $T_{bottom\ tank}$ would be a significant factor to analyze system performance.

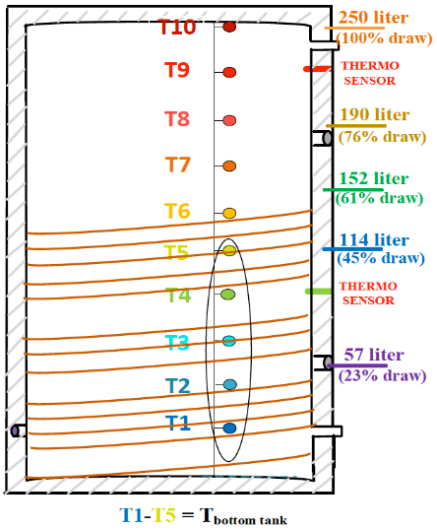

Figure 4.3 Location of each draw amount and definition of $T_{bottom\ tank}$

Figure 4.4 shows the temperature change under constant draw rate at 5 different draw amount. For 57 liter water draw, it could be noticed that there are 10 flat temperature lines with only T3 slightly increasing. This indicates little effect of the natural convection in the tank, as well as a good stratification. Because of the small draw amount and steady stratification, the sensor cannot touch the fresh water that cool enough to restart the heat pump. For the other four draw amounts, red dashed lines indicate the time when the heat pump restart automatically, the heat pump

restarts at the same time with the same draw rate. For higher draw amount, it requires more time for water temperature to recover.

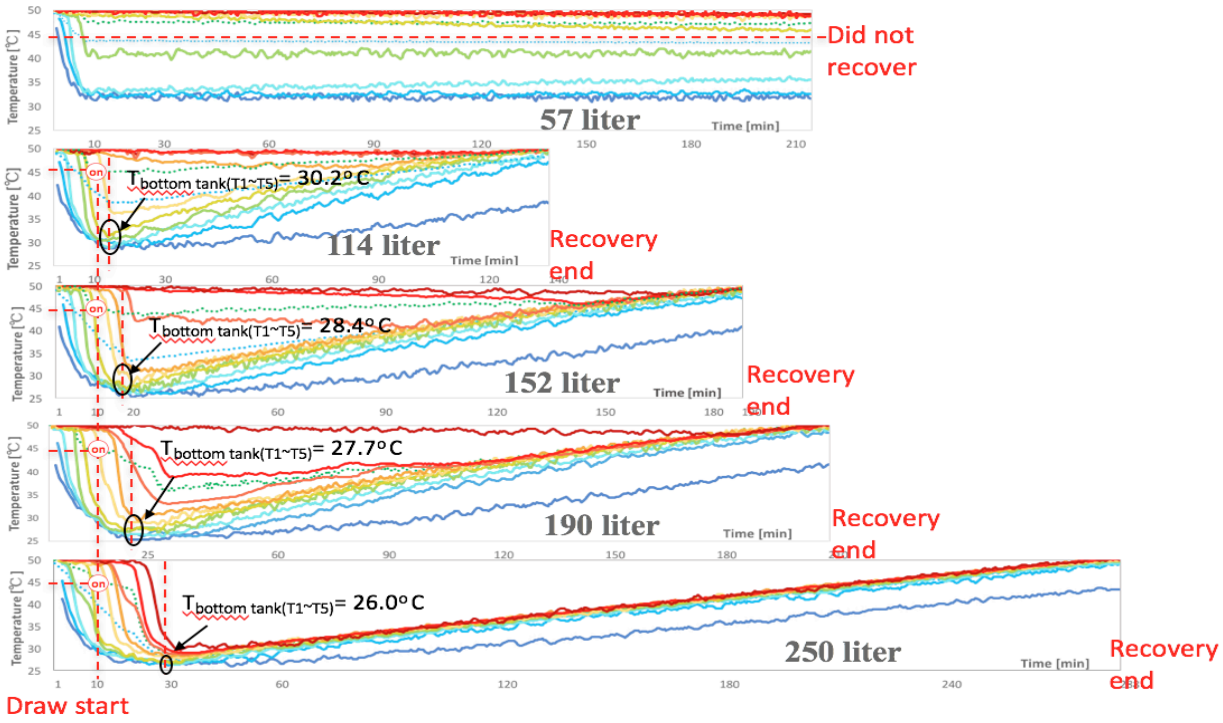

Figure 4.4 Vertical temperature change at 126 g/s draw rate, various draw amounts

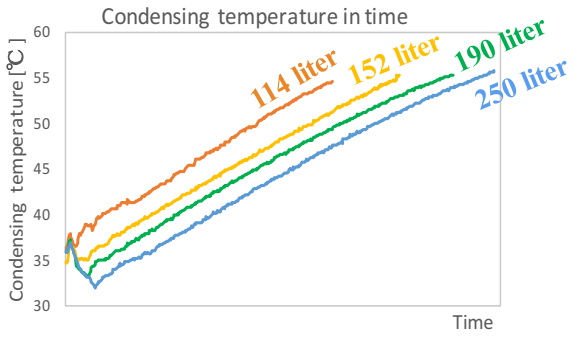

Figure 4.5 The cooler bottom tank results to lower condensing temperature

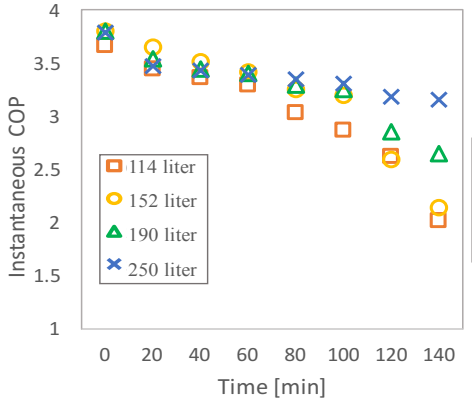

Figure 4.6 Instantaneous COP decreases with time

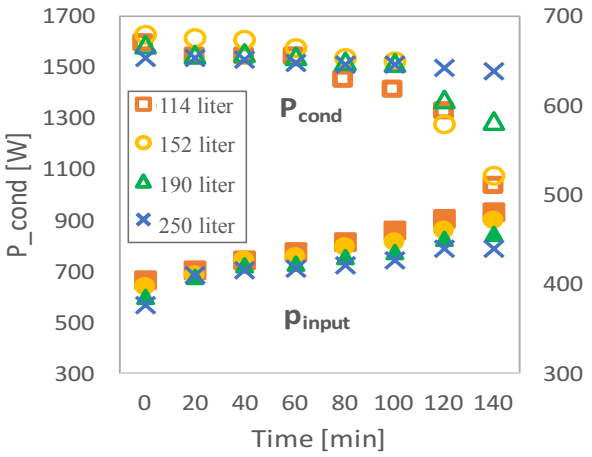

Figure 4.7 Compressor draws more power with time and condenser capacity decreases

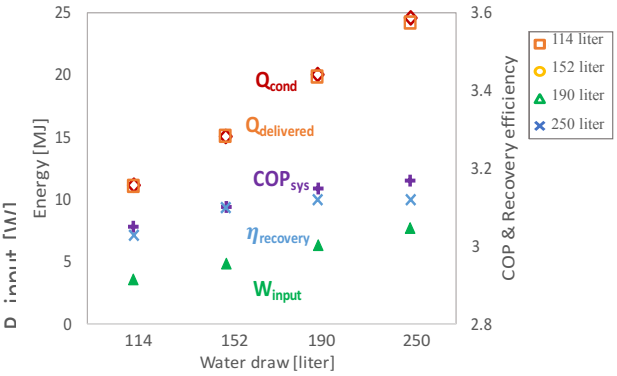

Figure 4.8 No significant effect (3%) of draw amount on HPWH performance

Figure 4.5 shows, the cooler bottom tank results to lower condensing temperature. Another factor that affects the performance is the height of the fresh cold water. The relationship between the height of the cold fresh water level and the topmost condenser coil will influence the condensing temperature. Compared the fresh cold water level of 114 l with other 152 to 250 l, the water level at 114 l draw is lower than the topmost wrapped around coil. The upper condenser coil will still conduct to the warmer water, which results in higher condensing temperature.

Figure 4.6 shows the instantaneous COP decreases with time. This is because as the water temperature increases, the head pressure at the compressor discharge is high due to higher condensing temperature with time. As Figure 11 indicates, this causes the compressor to draw more power, and the instantaneous rate of heat absorbed by the water in the wrapped around coil condenser decreases.

Figure 4.8 shows the values of two evaluations COP_{sys} and recovery efficiency. It appears that these two are the same evaluation metrics: the condenser capacity equals to the energy delivered at outlet, and recovery efficiency equals to the COP_{sys}. Both recovery efficiency and COP_{sys}

increase slightly with higher water draw (there is only a 3% efficiency increase from 114 to 250 l draw) which means that draw amount does not have a significant effect on the HPWH performance.

4.2 Effect of Draw Rate on HPWH Performance

Figure 13 shows the temperature change by constant draw amount with different draw rate changing from 25 to 189 g/s (0.4 gpm to 3 gpm). It indicates that longer time is required to recover the temperature at increasing draw rate. When the compressor starts, a warmer bottom tank is achieved at higher draw rate.

Figure 4.9 again validates the statement that the condensing temperature could be affected by the bottom tank condition. The higher draw rate that remains a warmer bottom tank temperature results to a higher condensing temperature.

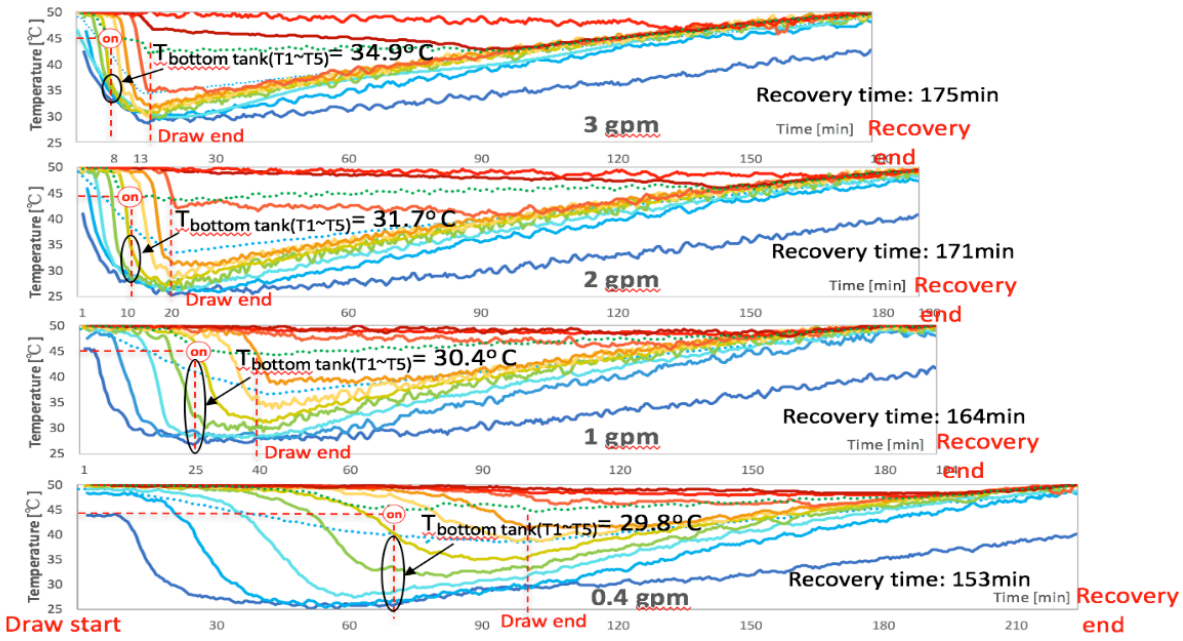

Figure 4.9 Vertical temperature measured by constant 152 l draw amount indicates a warmer bottom tank with higher draw rate when compressor restarts

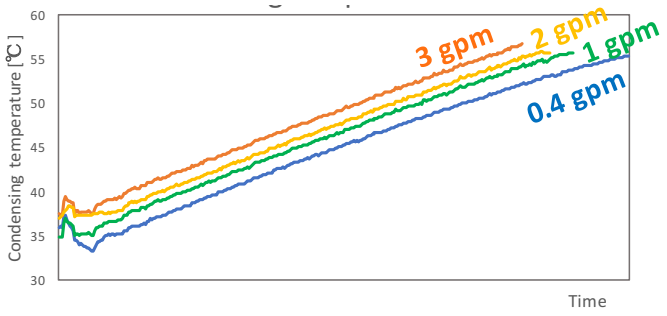

Figure 4.10 The warmer bottom tank results to a higher condensing temperature

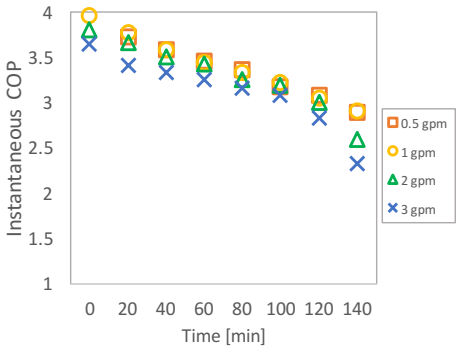

Figure 4.11 Instantaneous COP decreases with time

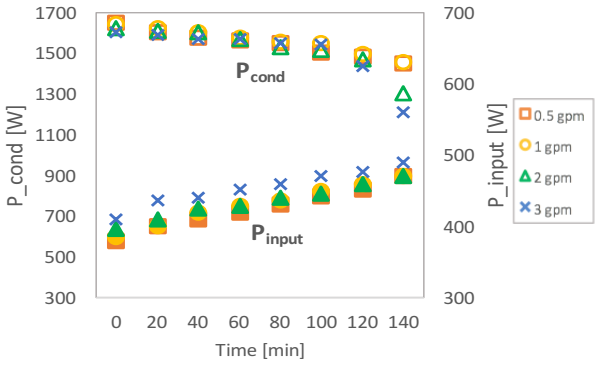

Figure 4.12 Compressor draws more power with time and condenser capacity decreases

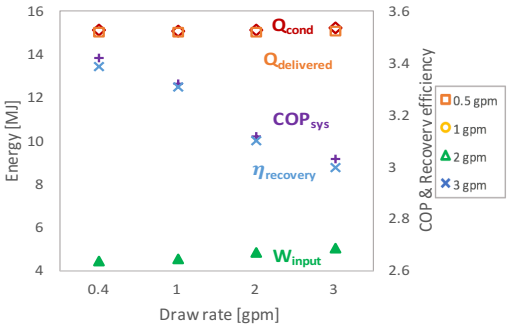

Figure 4.13 HPWH performance decrease (14%) with the increase of draw rate from 25 to 189 g/s (0.4 to 3 gpm)

Figures 4.11 and 4.12 show the instantaneous COP, condenser capacity and compressor power during the recovery period. It could be read from Figure 4.12 that higher draw rate requires compressor to draw more power while the condenser capacity remains almost the same, this results to a lower instantaneous COP shows in Figure 4.11.

Figure 4.13 again indicates the two evaluations COPsys and recovery efficiency coincide well with each other. It shows that with the same water draw amount, the energy delivered at the

outlet remains unchanged, so the system performance depends on how much electricity it used during the recovery period. With higher condensing temperature, the compressor draws more power, we could see there is a 14% recovery efficiency decrease from 25 to 189 g/s (0.4 to 3 gpm), which means that in order to bring the tank water back to the same condition as at the beginning, more electricity need to be used at higher draw rate.

4.3 Mixing in thermal storage tank

When adding same amount of cold water into the storage tank at different draw rate, each tank obtains the same internal energy. However, on a charge perspective, the tank with higher draw rate would achieve greater entropy generation and exergy due to the mixing. Figure 4.14 illustrates the entropy generation and exergy loss at different draw rate from 20 liters to 140 liters of the draw.

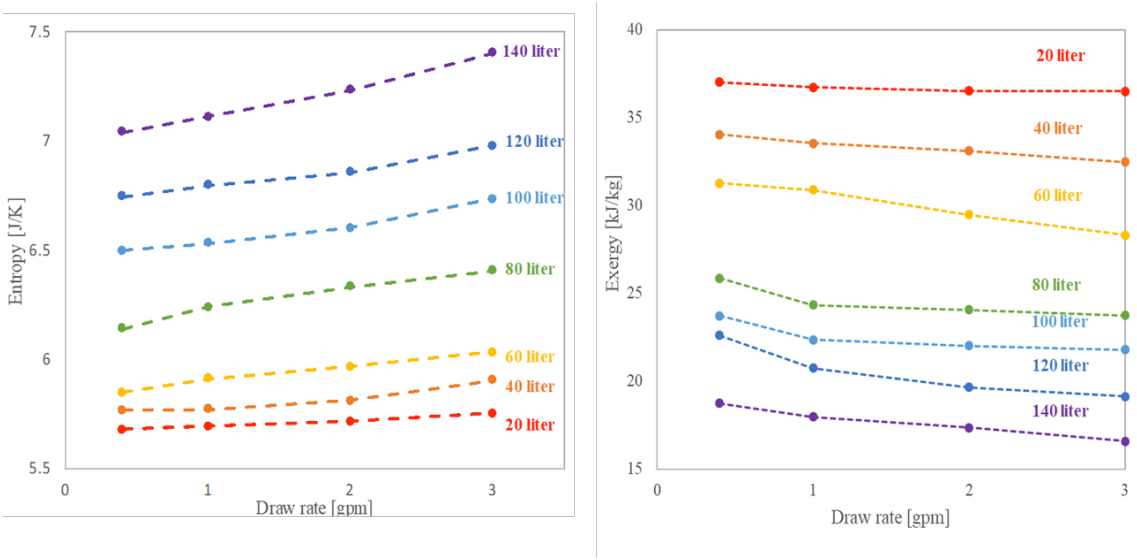

Figure 4.14 Higher draw rate causes more entropy generation and exergy loss

From Figure 4.14, it shows that the entropy increases and entropy decreases with the increment of draw rate, which indicates when drawing the same amount of water faster, more stratification would be destroyed and greater mixing happens in the storage tank. Furthermore, this trend

becomes more obvious with higher draw amount, entropy generates from 0.8% at 20 liters to 6% at 140 liters, while exergy losses from 1.1% at 20 liters to 12.2% at 140 liters.

Richardson number indicates the importance of natural convection relative to the forced convection. Lower Richardson number represents that the natural convection is negligible while larger Richardson number indicates forced convection can be neglected. In the HPWH storage tank, stratification is driven by the natural convection, and the inlet jet flow results in forced convection in the thermal tank.

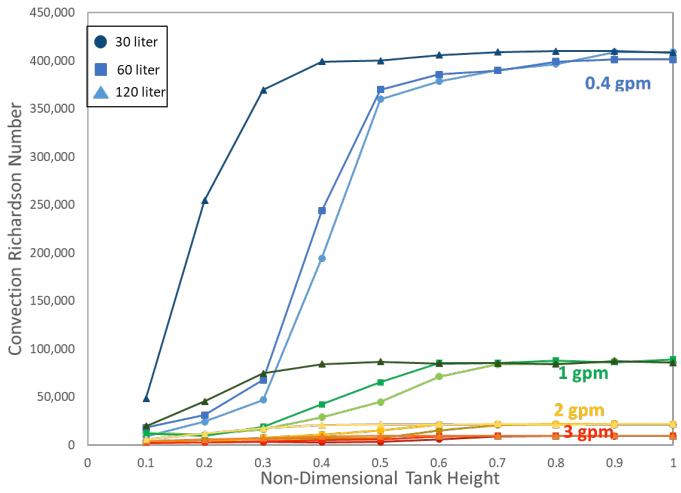

Figure 4.15 Lower Richardson number with draw rate indicates greater mixing in the storage tank

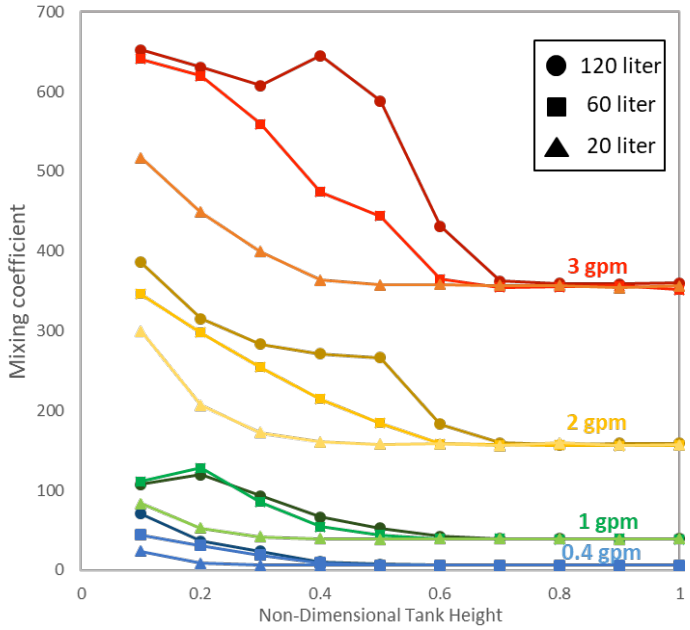

Figure 4.16 Higher mixing coefficient with draw rate indicates greater mixing in the storage tank

Figure 4.15 and 4.16 illustrates the Richardson number and mixing coefficient among the tank height at different draw rate from 0.4 gpm to 3 gpm. It could be found that higher draw rate obtains lower Richardson number and higher mixing coefficient, which indicates worse stratification and greater mixing. Furthermore, compared with bottom tank level, the upper tank obtains higher Richardson number as well as lower mixing coefficient, hence the upper tank remains lower mixing and better stratification since the inlet jet is located at the tank bottom.

When focusing on one certain draw rate, it could be noted that during the draw period at constant draw rate, the mixing in the lower tank level increases with the draw amount while the upper tank remains almost the same.

CHAPTER 5 – NUMERICAL MODELLING OF MIXING

5.1 Water Tank CFD Model

Three-Dimensional CFD model is carried out to explore the thermal tank mixing numerically. Figure 5.1 shows the geometry drawing of the thermal tank, the inlet and outlet are placed at the bottom and top, respectively. Table 5 lists the geometry parameters and the initial condition of the tank.

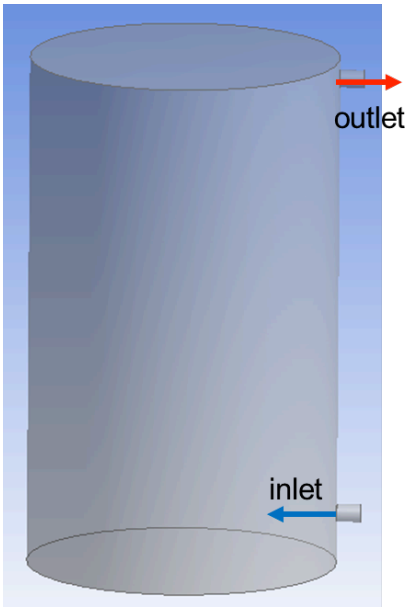

Figure 5.1 3D CFD tank model

Table 5.1 Water tank geometry and parameters

Tank height	106.0 cm
Tank OD	57.6 cm
Inlet height	10.0 cm
Outlet height	95.3 cm
Inlet OD	3.90 cm
Tank capacity	250 liters
Initial tank temperature	50 °C
Inlet water temperature	25 °C

In the CFD model, only the draw period is taking into consideration. The simulation start when the tank water is fully warmed up to the set point, and it is assumed that there is no temperature gradient at the start of the draw. Therefore, the initial tank temperature is set to be constant 50 °C, the cold water that enters from the inlet is set to be constant 25 °C.

The following assumptions have been made in the CFD model:

(a) Three-dimensional steady flow in the thermal storage tank;

(b) Laminar buoyancy driven flow in the thermal storage tank;

(c) The water density varies linearly with temperature, so the density change is polynomial.

The geometry is created in DESIGN MODELER and the mesh is generated in MESH, an approximately 500,000-element grid has been performed. Fluent 17.2 has been used as the CFD solver to obtain the temperature and velocity contour inside the tank. Based on the assumptions that made before, governing equations are solved by using Finite Volume Method and pressure based solver. SIMPLE (semi-implicit method for pressure-linked equations) scheme has been applied to pressure-velocity coupling, Green-Gauss Node Based has been chosen as the gradient, and Second Order scheme is used for the pressure accuracy. To improve the accuracy, Second Order Upwind has been applied for momentum and energy. The convergence standard has been taken as 1e-06 for the pressure residual, and for the continuity residual, 1e-3 has been selected. To better analyze the simulation data, CFD-Post has been used to plot the temperature and velocity distribution to predict the stratification level in the water tank during the draw period. Table 5.2 lists the calculation method for the model.

Table 5.2 Calculation method for CFD model

Pressure-velocity coupling	SIMPLE Scheme
Gradient	Green-Gauss Node Based
Pressure accuracy	Second Order Scheme
Momentum and energy	Second Order Upwind
Pressure residual	1e-06
Continuity residual	1e-04

5.2 Effect of Draw Rate on Mixing

Various draw rates from 1 to 3 gpm at same draw amount have been simulated based on the same tank configuration listed in Table 5.3 below.

Table 5.3 Simulation parameters of the draw rate effect

Draw rate	1/2/3 gpm
Inlet OD	3.9 cm
Inlet height	10 cm

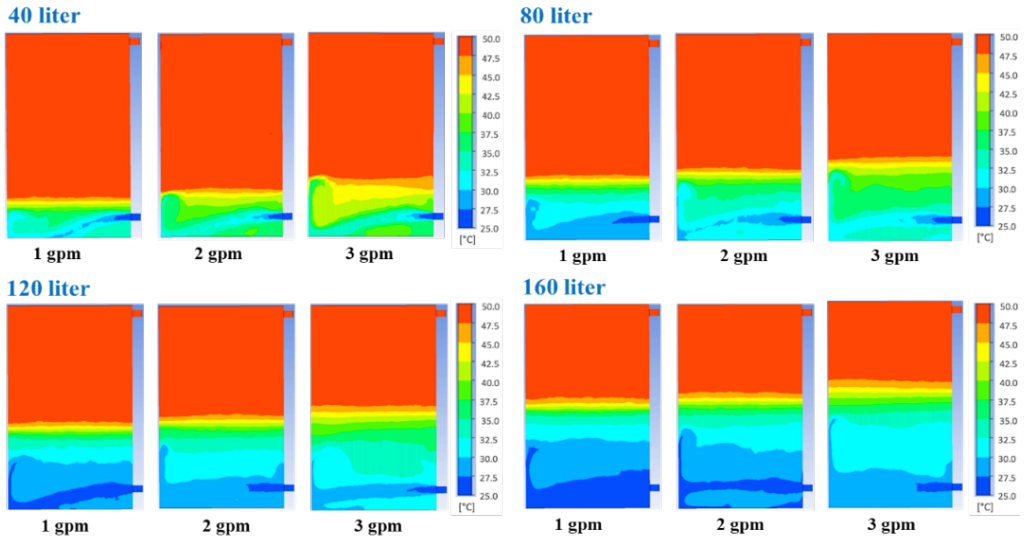

Figure 5.2 Temperature contours at different draw rates, in time during 152 l draw amount

Figure 5.2 illustrates the temperature contours for different draw rate from 0.15 to 0.35 m/s. As the cold water is discharging at higher rate than the water convection rate inside the tank, a free shear layer is developed results in mixing and entrainment of the surroundings.

With a smaller draw rate at the constant draw amount, the bottom tank obtains more blue area and the height of mixed water is lower. This indicates when slowly drawing the water, the cold water concentrates more at the bottom and hot water is kept in the tank as much as possible. It

coincides well with the experiment part that a warmer bottom tank would be achieved when drawing faster, which illustrate a worse stratification in the water tank.

5.3 Effect of Entrance Structure on Mixing

Another way to control stratification is by adding additional structures. In this paper, we consider the tank configuration with a baffle a little bit above the inlet, as well as an expanding nozzle connected to the tank inlet. Since the draw rate is determined by the user, on the manufacture side what we could do is reducing the inlet velocity by increasing the inlet surface area. Therefore, we consider the configuration with an expanding nozzle connected to the tank inlet which the diameter is two times of the original inlet diameter. We also considered another entrance structure with a baffle a little bit above the inlet, which the porosity is about 50%.

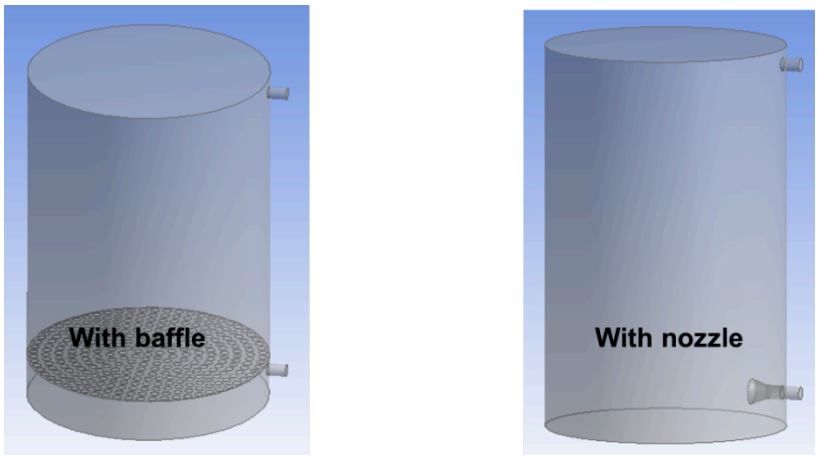

Figure 5.3 Geometry of two tank configurations with baffle and nozzle

Table 5.4 Simulation parameters of the entrance structure effect

Draw rate	2 gpm
Inlet OD	3.9 cm
Baffle porosity	50%
Nozzle OD	2 * Inlet OD

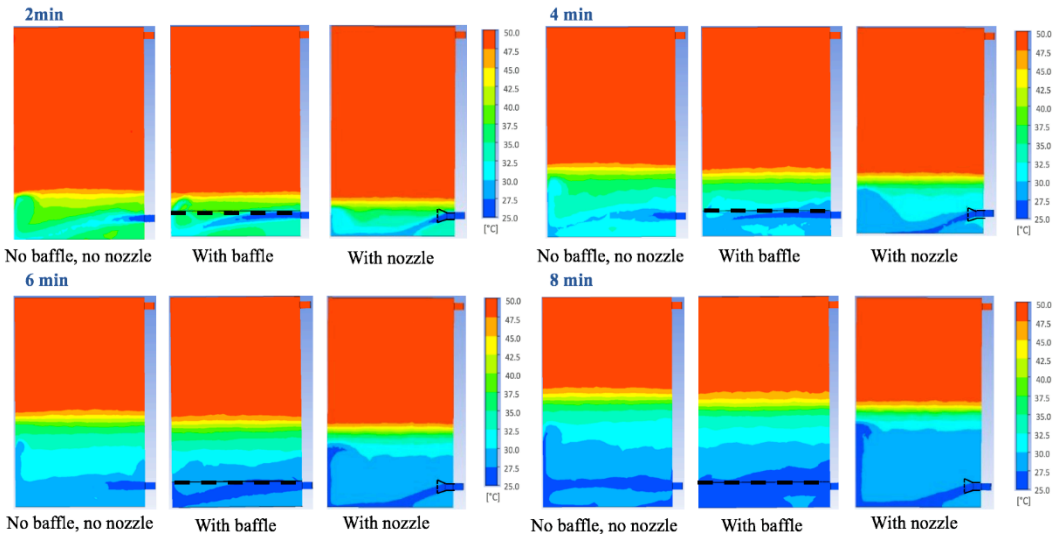

Figure 5.4 Temperature contours in three configurations, for 0.25m/s velocity at the inlet tube, in time during 152 liter total water draw amount (indicate less mixing with baffle or nozzle)

Figure 5.4 shows the temperature contours without baffle and nozzle, with only baffle and with only nozzle. It is obvious to find that with baffle and with nozzle, the height of mixed water is lower, which means more hot water is maintained in the tank. Without the baffle and nozzle, the cold water in the tank spreads more and destroys the tank stratification more. Besides, there is a larger low-temperature area below the baffle, which indicates the baffle controls mixing so that cold water could be limited to a smaller area. Compared with baffle and nozzle, the tank with nozzle remains a lower mixed water height during the draw period.

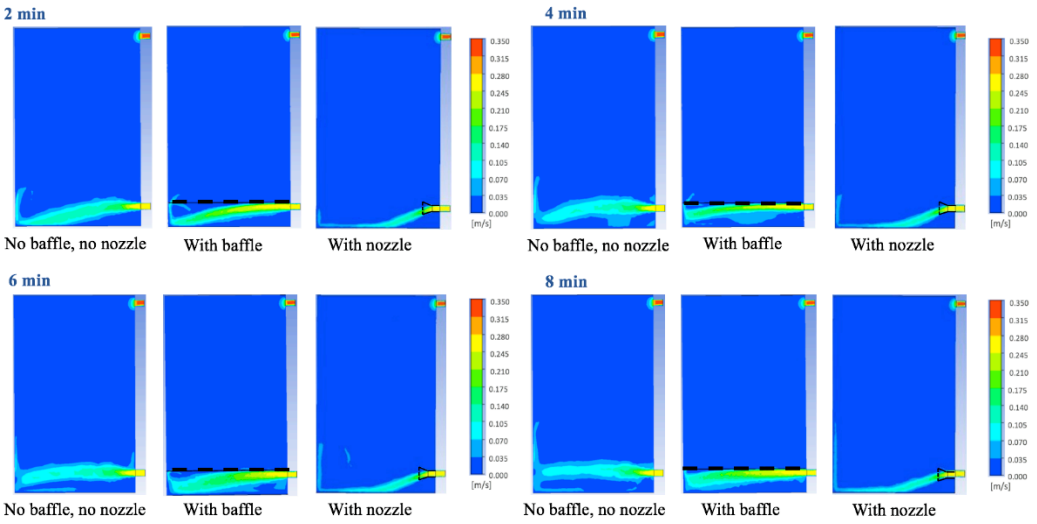

Figure 5.5 Velocity contours in three configurations, for 0.25m/s velocity at the inlet tube, in time during 152 l total water draw amount (indicate less mixing with baffle or nozzle)

Figure 5.5 shows the velocity contours without baffle and nozzle, with only baffle and with only nozzle. The one with nozzle has the lowest velocity gradient that it holds the smallest area where velocity is greater than 0. And the tank with nothing inside holds the largest velocity gradient area. Therefore, the conclusion can be drawn that by limiting the mixing near the inlet area and reducing the inlet velocity, the tank stratification could be maintained better.

The convection Richardson number at non-dimensional tank height with different entrance structures is given in Figure 5.6.

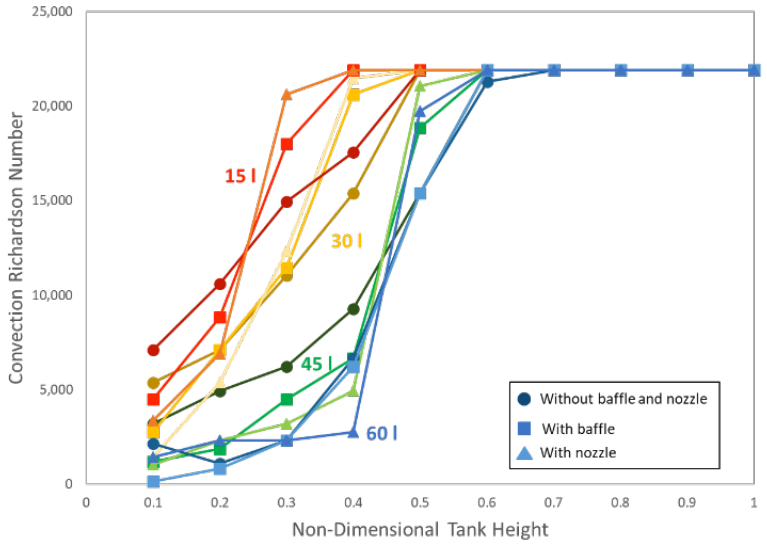

Figure 5.6 Highest Ri number with nozzle and lowest Ri number without any entrance structures

Richardson number remains the same at the upper level of the tank, which indicates same mixing at the hot water area where no mixing happens. It clearly shows that the tank with nozzle obtains the highest Ri number at each draw amount that it holds the best stratification and minimize the mixing in the storage tank.

5.4 Effect of Inlet Location on Mixing

Another way of promoting stratification by tank design is the inlet location. Table 5.5 lists the parameters that used in the simulation of different inlet location effect.

Table 5.5 Simulation parameters of the inlet location

Draw rate	2 gpm
Inlet OD	3.9 cm
Inlet height	5/10/15 cm

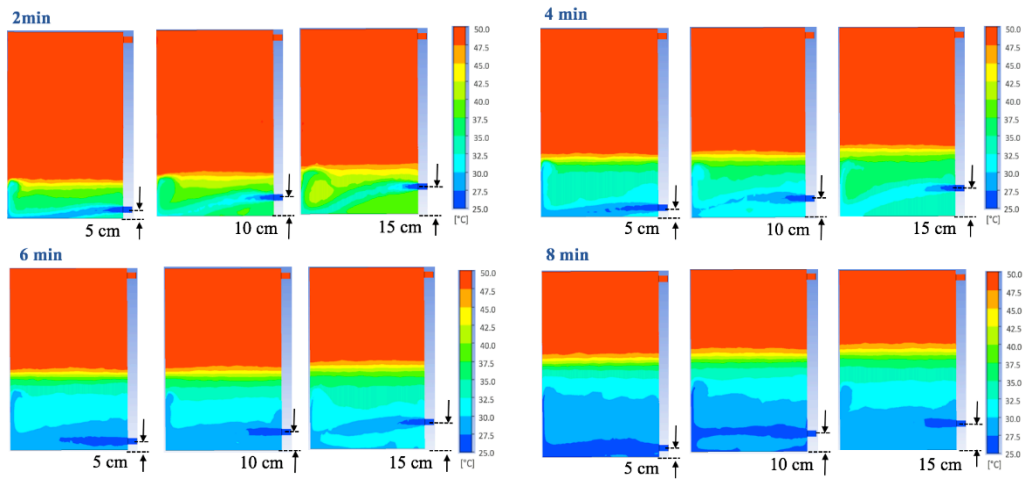

Figure 5.7 Temperature contours in three inlet positions, for 0.25m/s velocity at the inlet tube, in time during 152 l total water draw amount

As it shown in figure 5.7, three different inlet locations are considered in this paper, 5cm, 10cm and 15cm away from the tank bottom respectively. Lower inlet position obtains larger cold area at the bottom and larger hot water at upper tank, indicates that the stratification is directly impacted by the inlet design, in order to have less mixing and better stratified tank, the inlet should be placed as close as possible to the tank bottom.

CHAPTER 6 – EXPERIMENT ON REFRIGERANT SIDE

6.1 Experimental bench and procedure

6.1.1 Experimental Facility

Figure 6.1 illustrates a schematic drawing of the HPWH system and the experimental setup. It is a similar HPWH that is illustrated in Chapter 2, which contains a fin and tube evaporator, a rotary compressor, a low-pressure side accumulator, an electronic expansion valve, a wrap-around coil condenser, and a water tank. Since the superheat degree is supposed to be maintained by regulating the steps of the EEV but it cannot be always guaranteed, the accumulator is placed at the inlet of the compressor to avoid any impact of the refrigerant.

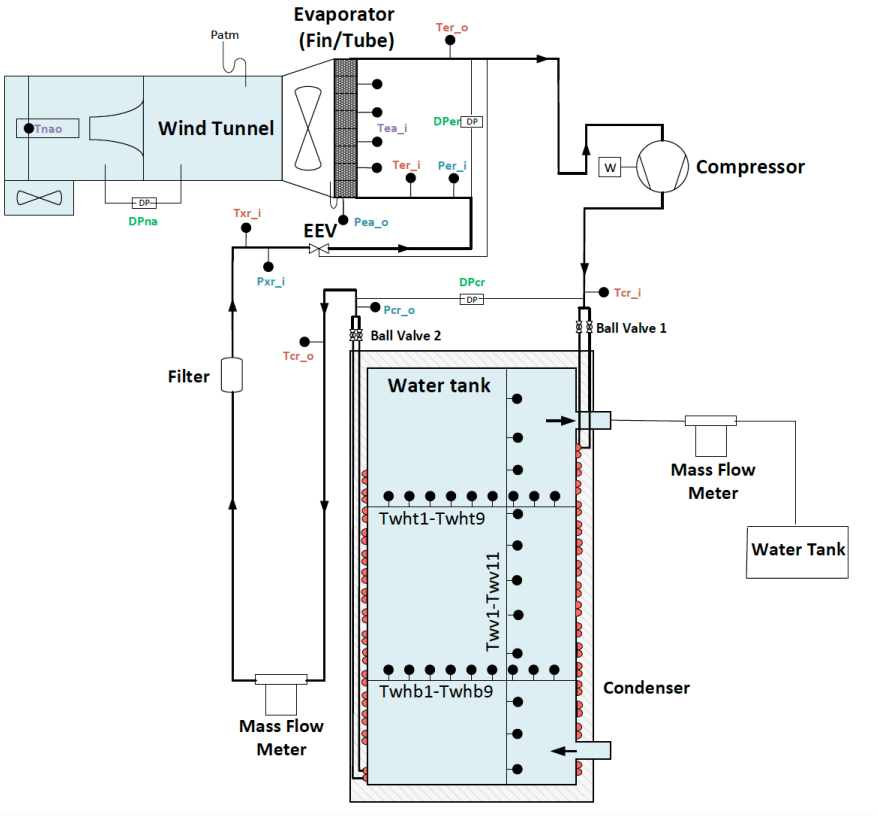

Figure 6.1 Schematic drawing of experimental facility

The system tested is an R134a based Heat Pump Water Heater system, and four system were tested:

(a) the baseline R134a HPWH system with two-circuit condenser

(b) the same system as (a), operating with an optimal charge of R1234yf with the baseline rotary compressor and EEV setting

(c) the baseline R134a HPWH system with one-circuit condenser

(d) the same system as (c), operating with an optimal charge of R1234yf with the baseline rotary compressor and EEV setting

In order to implement a one-circuit condenser, 4 manually operated ball valves are installed in the two refrigerant loops at the inlet and outlet of the condenser. Therefore, by closing two of the ball valves of the inlet and outlet from the same circuit, this condenser circuit can be bypassed and only one circuit is connected to the system.

6.1.2 Experiment Procedure

For the purpose to obtain and compare the performance of two refrigerants and condenser circuits, a fair test condition should be carried out. Therefore, all four tests are performed with the fixed external fixed heat transfer fluids (water and air) temperature, the evaporation and condensation saturation temperatures have been remained the same for each test. The operation contains a fully warm-up period to heat the water from 25℃ to 50℃.

Firstly, tests are conducted for R134a with the original two-circuit condenser, then comes with the subsequent tests conducted with the same system component design as well as external conditions for the drop-in refrigerant 1234yf. After that, R134a and R1234yf with one-circuit condenser are performed under the same operation condition.

6.2 Performance Evaluation Method

The performance and behavior of the HPWH system are calculated with the experimentally measured data. Evaporating and condensing temperatures are obtained by calculating the saturated conditions with the pressures at the evaporator inlet and condenser outlet. Condenser subcooling and evaporator superheat are calculated through Equation (6.1) and (6.2), respectively.

$$T_{SC} = T_{cr,sat} - T_{cr,o} \tag{6.1}$$

$$T_{SH} = T_{er,o} - T_{er,sat} \tag{6.2}$$

Condenser capacity and cooling capacity is calculated with Equation (6.3) and (6.4), the expansion process is assumed to be isentropic.

$$\dot{Q}_{cr} = \dot{m}_r * \Delta h_{cr} = \dot{m}_r * (h_{cr,o} - h_{cr,i}) \tag{6.3}$$

$$\dot{Q}_{er} = \dot{m}_r * \Delta h_{er} = \dot{m}_r * (h_{er,o} - h_{er,i}) \tag{6.4}$$

Where, $\dot{Q}_{cr}$ and $\dot{Q}_{er}$ are the heating and cooling capacity, $\dot{m}_r$ is the measured refrigerant mass flow rate, $h_{cr,i}$ and $h_{cr,o}$ are the refrigerant specific enthalpy at the condenser inlet and outlet, $h_{er,i}$ and $h_{er,o}$ are the refrigerant specific enthalpy at the evaporator inlet and outlet.

Air side capacity can be calculated based on Equation (6.5).

$$\dot{Q}_{ea} = \dot{m}_{air} * (h_{ea,i} - h_{na,o}) \tag{6.5}$$

Where, $h_{ea,i}$ and $h_{na,o}$ are the enthalpy before and after passing through the evaporator. Air stream temperature are measured before and after passing through the evaporator to obtain the air enthalpy. $\dot{m}_{air}$ is the air flow rate that obtained and calculated by the differential pressure transducer in the nozzle.

COP can be used as a criteria to evaluate the performance of the HPWH. Equation (6.6) defines the COP during the warm-up operation, as the ratio of condenser capacity to the compressor consumption. It is the quotient between specific heating and specific compressor consumption.

$$\mathrm{COP} = \frac{Q_{cond}}{W_{comp}} \tag{6.6}$$

Besides, the refrigerant mass flow rate, compressor discharge temperature, compressor power consumption are measured directly from the transducers that installed in the HPWH system.

CHAPTER 7 – EXPERIMENTAL RESULTS ON REFRIGERANT SIDE

This chapter describes the experimental results that obtained using different refrigerant R134a and R1234yf, as well as the hardware modification on the condenser circuit.

7.1 R134a vs R1234yf

Table 7.1 lists the drop-in test results for R134a and R1234yf. Tests are conducted at least two times for the accuracy.

Table 7.1 Average COP, cooling capacity, compressor discharge temperature, charge and heating-up time for R134a and R1234yf

Refrigerant	COP	Diff. COP (%)	Q_e (kW)	Diff. Q_e (%)	$T_{dis.}$ (°C)	Diff. $T_{dis.}$ (°C)	Charge (g)	Operation time (min)
R134a	4.42	-8.2	1.45	-11	59.5	-6.8	825	208
R1234yf	4.03		1.29		55.4		785	225

The average COP and cooling capacity for R1234yf is approximately 8.2% and 11 % lower than baseline R134a, respectively. While the measured compressor discharge temperature for R1234yf is 6.8℃ lower than those of R134a. Finally, the amount of refrigerant charge for R1234yf is 5% lower than those obtained for R134a due to the density decrease of R1234yf. The operation time using R1234yf is 8% higher than that of R134a to warm up the water from 25℃ to 50℃.

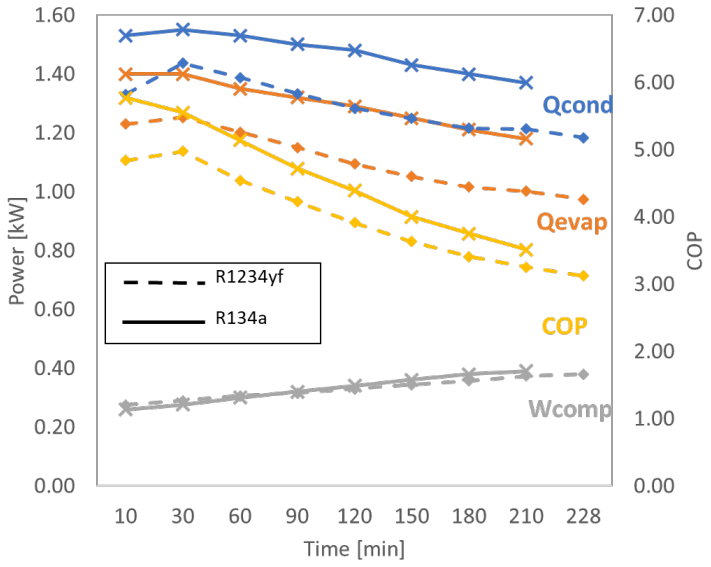

Figure 7.1 lower capacity and COP for R1234yf

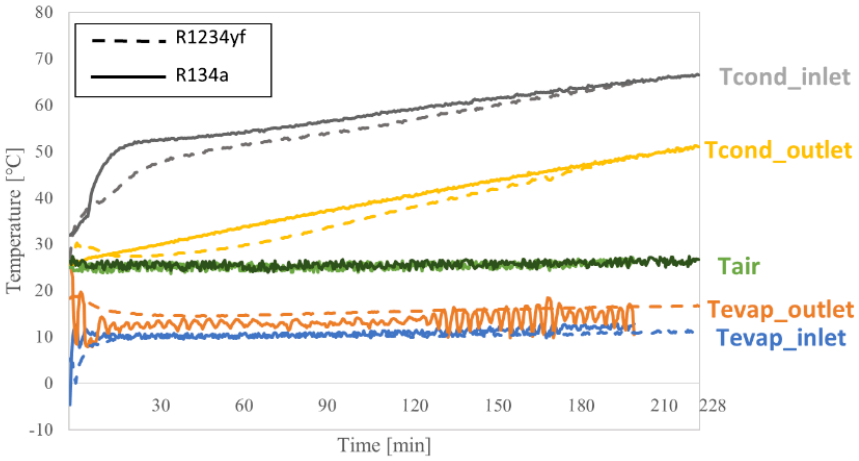

Figure 7.2 Compressor discharge temperature is up to 10% lower for R1234yf than R134a

Figure 7.1 presents the power and COP using both refrigerants at same working conditions.

Figure 7.2 shows the refrigerant side temperature for both refrigerants. It can be seen that the temperatures at the condenser inlet and outlet for R1234yf are up to 10% lower than using R134a, and the slope for R1234yf is sharper so that the temperature difference between two refrigerants becomes smaller with time. Furthermore, since the compressor discharge

temperature is slightly lower for R1234yf than R134a, a similar compressor configuration and current compressor lubricant can be feasible to use for the drop-in refrigerant.

It is noted that the compressor power consumption increases with the increase of condensation temperature, which can be explained by the rise of compression ratio. The slope of the compressor power obtained by R134a is sharper than that of R1234yf.

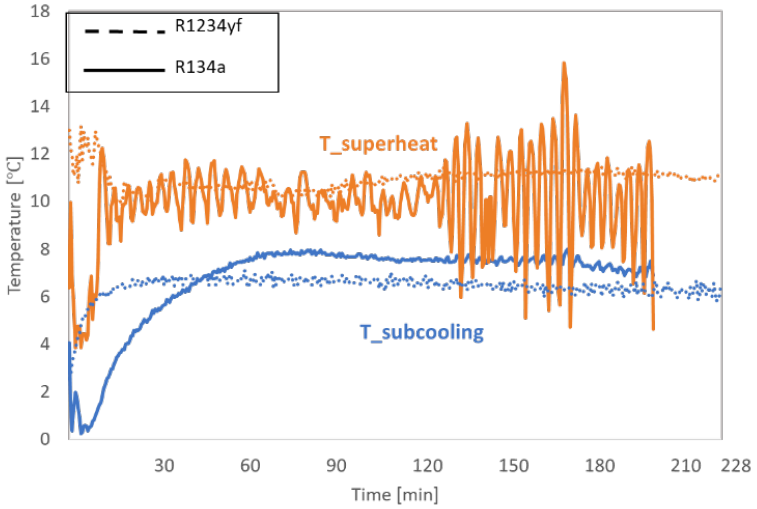

Figure 7.3 0.8℃ higher superheat in evaporator and 2℃ lower subcooling in condenser

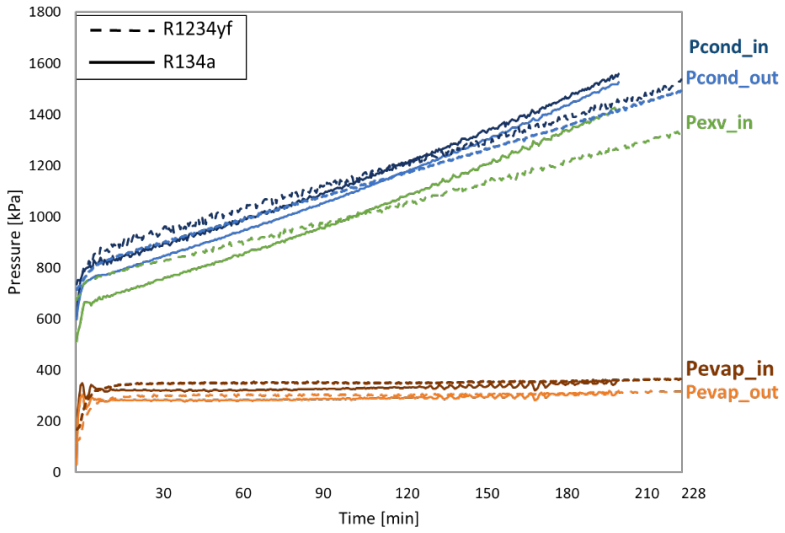

Figure 7.4 Pressure in each component using R134a and R1234yf

The heat rejection rate for R1234yf is approximately 10% lower, with 1.5-2 ℃ lower liquid subcooling and higher condenser inlet pressure. Meanwhile, the pressure drop and the saturation temperature drop through the condenser for R1234yf remains almost the same with R134a, which clearly indicates that R1234yf could be used in the same condenser design as a drop-in refrigerant, and it may benefits more from an improved design.

On the evaporator side, the larger R1234yf saturation temperature drop (2.5 ℃ greater) at almost same superheat degree (0.8℃ higher), the R1234yf could benefit from a redesigned evaporator.

The refrigerant mass flow rate measured directly by the Coriolis mass flow meter, and it is a function of several variables in accordance with Equation (7.1).

$$\dot{m}_{ref} = \frac{\eta_v \cdot V_{comp} \cdot N}{v_{comp,in} \cdot 60} \tag{7.1}$$

Where, η_v is the compressor volumetric efficiency, V_{comp} is the geometrical volume that only relies on the compressor geometrical dimensions. N is the compressor rotation speed, $v_{comp,in}$ is the specific volume at compressor inlet. For a fixed compressor, the mass flow rate that measured in the experiments only relies on the volumetric efficiency and specific volume at compressor inlet.

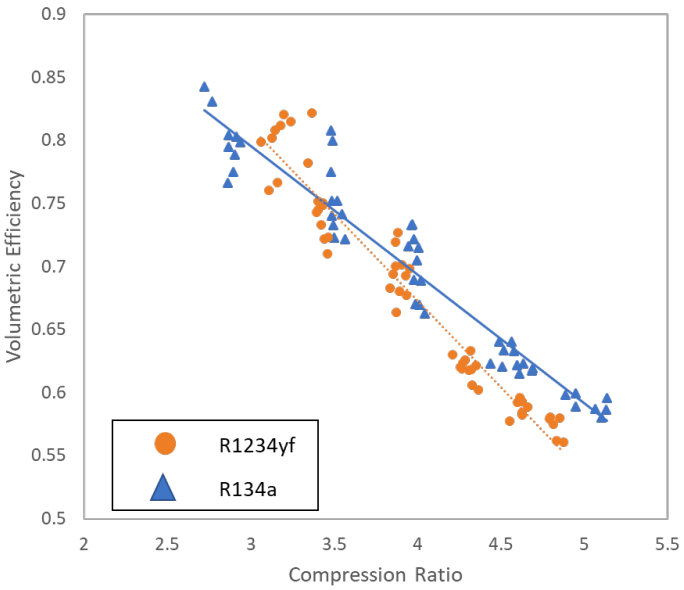

Figure 7.5 Volumetric efficiency versus compression ratio using R134a and R1234yf

Figure 7.5 indicates the effect of compression ratio on the compressor volumetric efficiency when using R134a and R1234yf. It can be observed that the volumetric efficiencies of two refrigerants are relatively close (with difference ranging between 0.4% and 5%), with lower compression ratio, the volumetric efficiency for R1234yf is slightly higher than that of R134a, and is up to 5% lower compared with R134a when compression ratio is over than 3.5. Furthermore, it can also be noted in this figure that the points' dispersion for R1234yf is larger than that obtained for R134a, which indicates that higher pressure drops when using R1234yf would cause a larger influence of compressor speed on volumetric efficiency.

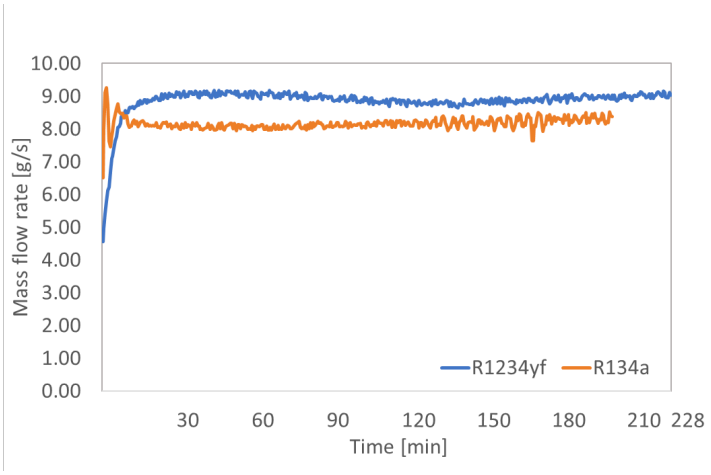

Figure 7.6 Refrigerant mass flow rate for R1234yf is up to 15% higher than that of R134a

The refrigerant mass flow rate driven by the compressor with R1234yf is higher (by up to 15%) than R134a, since R1234yf does not introduce a significant volumetric efficiency difference, and it obtains higher suction density as well as lower specific volume, higher mass flow rate is driven by the compressor.

Entropy generation for each component can be specified from below:

$$\delta S_{evap} = \dot{m}\left(s_{er,o}\text{-}s_{er,i}\right)\text{-}\frac{\dot{Q}_e}{T_e} \tag{7.2}$$

$$\delta S_{cond} = \dot{m}\left(s_{cr,o}\text{-}s_{cr,i}\right)\text{-}\frac{\dot{Q}_c}{T_c} \tag{7.3}$$

$$\delta S_{comp} = \dot{m}\left(s_{cr,i}\text{-}s_{er,o}\right) \tag{7.4}$$

$$\delta S_{eev} = \dot{m}\left(s_{er,i}\text{-}s_{cr,o}\right) \tag{7.5}$$

The entropy generation of the total HPWH system equals to the sum of all the entropy generations above:

$$\sum \delta S_{total} = \delta S_{evap} + \delta S_{cond} + \delta S_{comp} + \delta S_{eev} \tag{7.6}$$

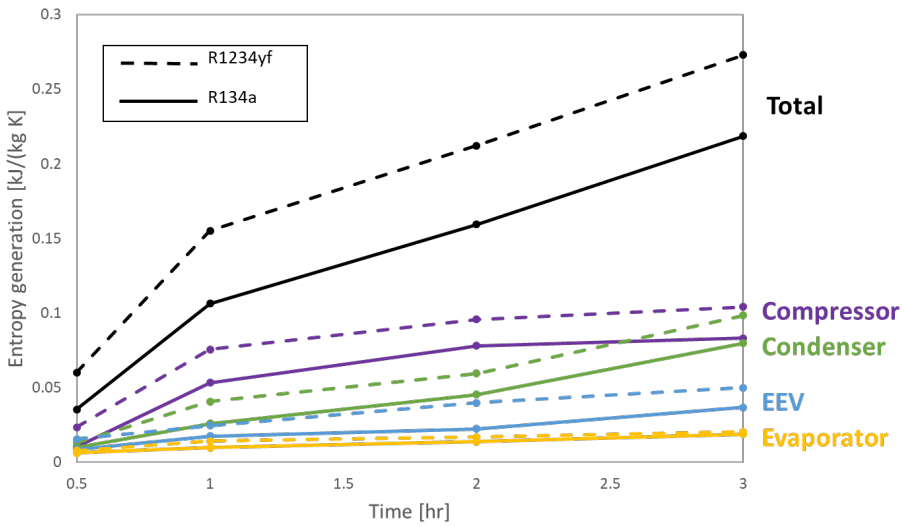

Figure 7.7 System using R1234yf generates 31% more entropy than R134a in total

Compressor has the highest amount of entropy generation in both cycles so that about 50% of the total entropy production is accumulated to the compressor.

The entropy generates more when the heat loss in the condenser increases, which indicates a lower condenser inlet temperature. The entropy generation obtained with R1234yf is 25% higher than that of R134a, this is because as the compressor discharge temperature decreases with R1234yf, the heat loss from the condenser increases.

Since entropy generation for individual components is higher when using R1234yf, therefore the total entropy generation of 1234yf is 31% more than that of 134a.

The results indicates that entropy analyses can be used as a proper method to determine the occurrence point of the maximum loss and system irreversibility.

7.2 Effect of Condenser Circuit Number Using R134a

Table 7.2 Average COP, cooling capacity, compressor discharge temperature, charge and heating-up time for one-circuit and two-circuit condenser using R134a

Circuit	COP	Diff. COP (%)	Q_e (kW)	Diff. Q_e (%)	$T_{dis.}$ (°C)	Diff. $T_{dis.}$ (°C)	Charge (g)	Operation time (min)
one	4.26	-3.7	1.44	-0.7	56.6	1.2	625	218
two	4.42		1.45		55.4		830	208

Table illustrates the performance results on one-circuit and two-circuit condenser with R134a. The average COP and cooling capacity for one-circuit decreases 3.7%, while cooling capacity decreases only 0.7%. The compressor temperature is 1.2℃ higher than that of two-circuit, and the charge for one-circuit condenser system is 24.6% lower than that of two-circuit, it takes 4.6% shorter operation time for the one-circuit system to heat up the water from 25 ℃ to 50 ℃.

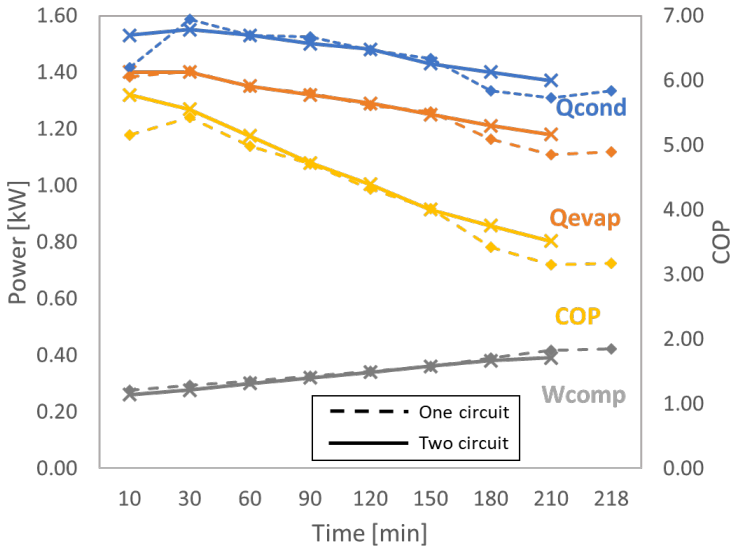

Figure 7.8 Power and COP for one-circuit is lower than that of two-circuit in the first and last hour of heating operation

Figure 7.8 indicates the power and COP for two condenser designs during the operation. In general, two curves looks almost the same. In the first 30 minutes, there is up to 4% increase for the one-circuit compressor work, 7.3% and 12.2% decrease in condenser capacity and COP,

respectively. In the middle period of the operation, there is no obvious difference between two condenser designs, and in the last 60 minutes, the condenser capacity, cooling capacity for one-circuit condenser system decrease up to 4% and 7% respectively, while compressor work increases up to 4%, these cause the COP drops up to 7.4% compared with the original two-circuit condenser system.

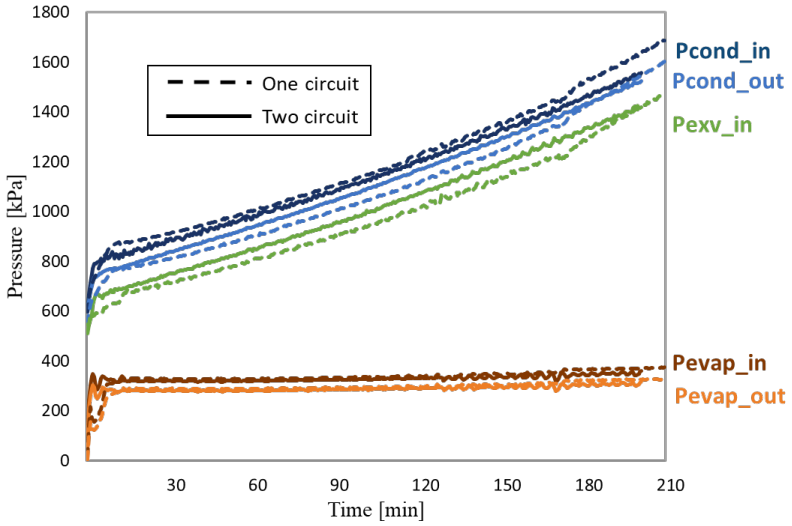

Figure 7.9 Higher pressure drop in condenser and liquid line for one-circuit condenser system

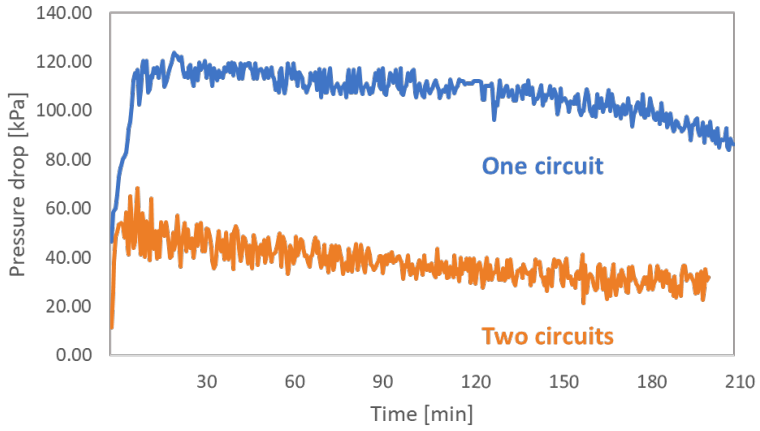

Figure 7.10 Pressure drop in the one-circuit condenser is two times of the two-circuit

Figure 7.9 and 7.10 illustrate the pressure at each component and the pressure drop during the heating process. The difference of the pressure between one-circuit and two-circuit at evaporator inlet and outlet are within 2%, while the pressure at EEV inlet for one-circuit is 6% lower than that of two-circuit, which indicates the pressure drop at liquid line is higher when using one-circuit condenser.

The two-circuit design helps to minimize the pressure drop in the condenser, one-circuit condenser causes a large pressure drop since it decreases the condenser tube size, which in turn results in lower saturation temperature and hence drops the performance.

The condenser obtains a higher inlet pressure and lower outlet pressure compared with the original two-circuit design, the pressure drop in the condenser for one-circuit increases 157%.

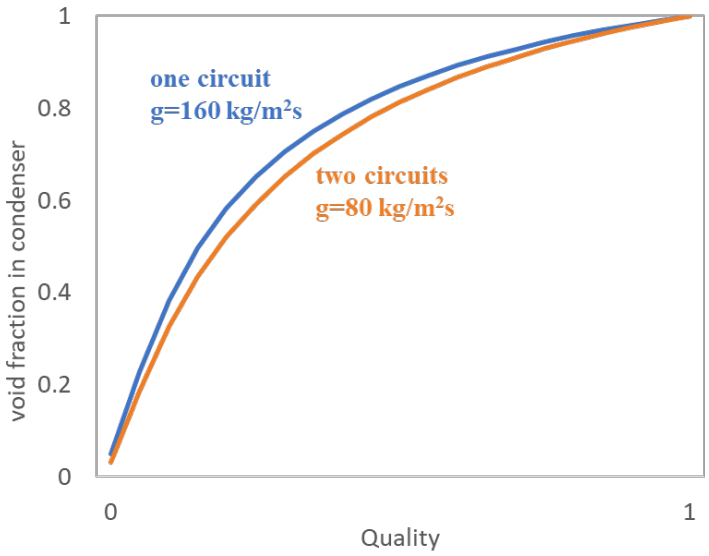

Figure 7.11 Higher void fraction in condenser for one-circuit condenser

Figure 7.11 shows the void fraction with quality in the condenser. In general, the quality and void fraction decrease continuously along the condenser tubes, the mass flux *g* and void fraction α are obtained by Equation (7.7) and (7.8)

$$g = \frac{\dot{m}_r}{A} = \frac{\dot{m}_r}{\pi d^2/4} \tag{7.7}$$

$$\alpha = \frac{1}{1+\frac{1-x}{x}\frac{\rho_g}{\rho_v}S} \tag{7.8}$$

Where, $\dot{m}_r$ is the refrigerant mass flow rate, A is the cross-sectional area of the condenser tube, x represents the flow quality and S is the slip ratio.

Here, 1 represents the superficial quality which indicates the moment when liquid shows up at inner wall of the condenser. Since the mass flux depends on refrigerant mass flow rate and the cross-sectional area of the condenser tube, it is obvious that two-circuit condenser obtains lower refrigerant mass flux than that of one-circuit due to the increase of cross-sectional area, which indicates a higher refrigerant charge for two-circuit system. Figure and experimentally proves that the pressure drop across the condenser section rises with the increase of the refrigerant mass flux.

Larger cross-sectional area is occupied by the vapor phase for one-circuit condenser.

P-h diagram of the warm-up period for two condenser configurations are given in Figure 7.12. In general, for both two condensers, the condensation pressure and condensation temperature increases with time due to the heating up process on the water side. The degree of liquid subcooling also generates more with condensation pressure, this can be explained by the sharper liquid phase curve of R134a. For both condenser configurations, during the heating up process, only slightly increase on the evaporation temperature and pressure due to the constraint ambient temperature and condition. Relatively constant vapor superheat is obtained for both systems because of the control of the Electronic Expansion Valve.

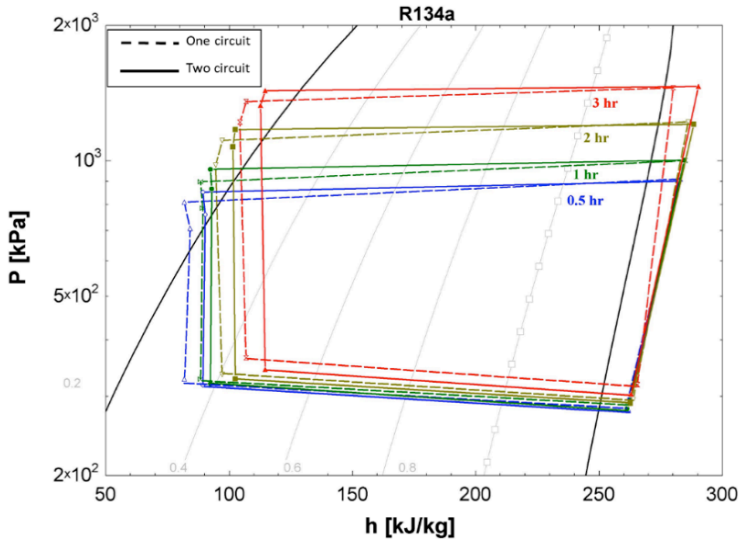

Figure 7.12 Development of the system operating condition for one-circuit and two-circuit condensers: higher condensation temperature and lower evaporation temperature for two-circuit condenser system

Comparing the P-h diagram of one-circuit condenser system with the two-circuit, same constant vapor superheat value is obtained, the liquid subcooling for one-circuit condenser is higher. Furthermore, one-circuit condenser system gains a higher evaporation temperature and lower condensation temperature compared to the original two-circuit design.

7.3 Effect of Condenser Circuit Number Using R1234yf

Same experimental procedures are taken by using R1234yf to see the effect of condenser circuit number on system performance. Some experimental results are given in Table 7.3.

Table 7.3 Average COP, cooling capacity, compressor discharge temperature, charge and heating-up time for one-circuit and two-circuit condenser using R1234yf

Circuit	COP	Diff. COP (%)	Q_e (kW)	Diff. Q_e (%)	$T_{dis.}$ (°C)	Diff. $T_{dis.}$ (°C)	Charge (g)	Operation time (min)
one	3.81	-5.5	1.28	-0.77	60.66	1.16	595	234
two	4.03		1.29		59.5		775	225

Table 7.3 illustrates the performance results on one-circuit and two-circuit condenser with R1234yf. Similar to R134a, the average COP and cooling capacity for one-circuit decreases 5.5%, while cooling capacity decreases only 0.77%. The compressor temperature is 1.16℃ higher than that of two-circuit, and the charge for one-circuit condenser system is 23.2% lower than that of two-circuit, it takes 4.0% shorter operation time for the one-circuit system to heat up the water from 25 ℃ to 50 ℃.

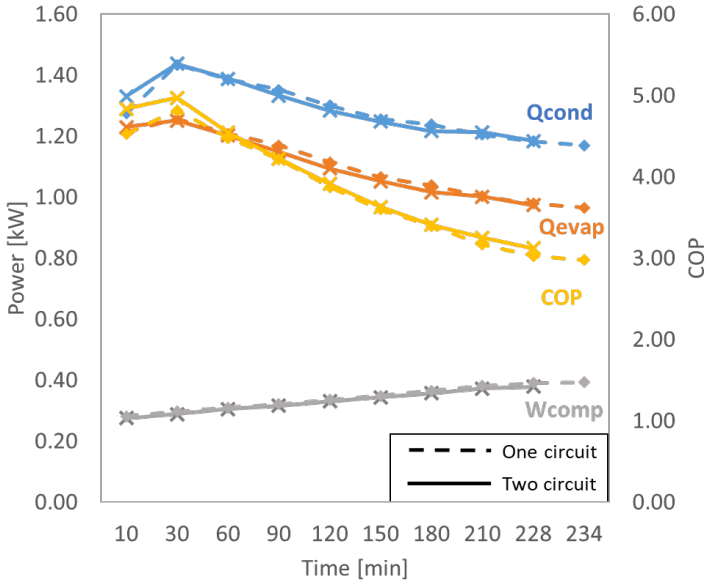

Figure 7.13 The difference of power and COP between one circuit and two using R1234yf is within 5%.

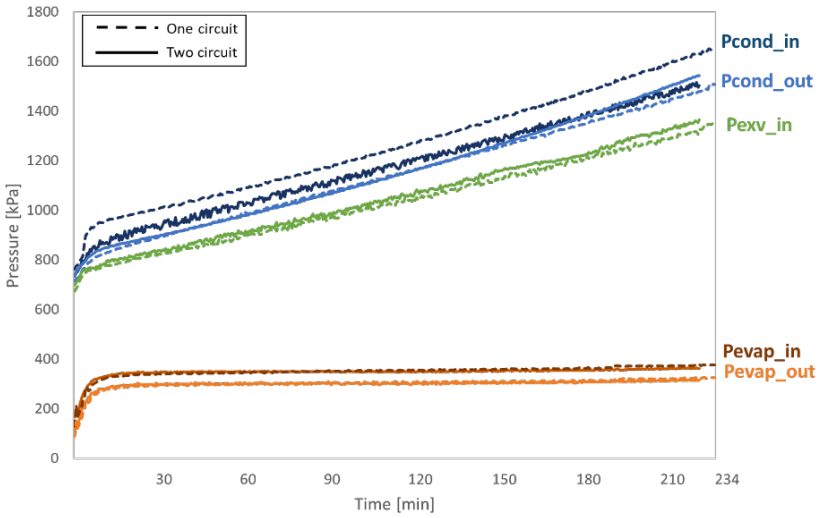

Figure 7.14 Higher pressure drop in condenser and liquid line for one-circuit condenser system using R1234yf

Figure 7.14 shows that for the one-circuit system, the discharge pressure is higher than that of two-circuit condenser system, ranges between 6.3% and 8.1%. Pressure at condenser outlet is slightly higher (within 2.7%) for one-circuit system at the later stage of heating process. Since there is no modification for the evaporator, the pressure at its inlet and outlet remain the same.

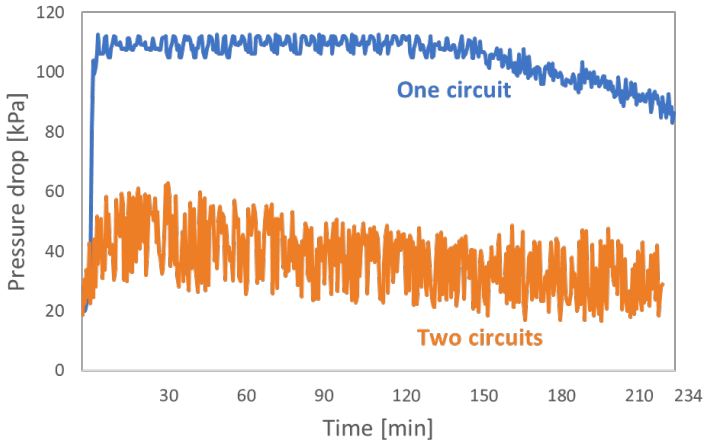

Figure 7.15 Pressure drop in one-circuit condenser is almost two times of the two-circuit condenser

Figure 7.15 shows the pressure drop in both condenser configuration using R1234yf. Same as the R134a system, one-circuit condenser obtains a large pressure drop since it decreases the condenser tube size, which in turn results in lower saturation temperature and hence drops the performance.

The condenser obtains a higher inlet pressure and lower outlet pressure compared with the original two-circuit design, the pressure drop in the condenser for one-circuit increases 160%.

CHAPTER 8 – SYSTEM PERFORMANCE MODELLING

8.1 Model Overview

Modeling a HPWH system is a challenge due to the complexity of various sub-systems and the integration between the vapor-compression cycle and the water tank. Therefore, a EES-Fluent linked model has been developed and used to simulate and validate the transient heating-up process of the HPWH system. The CFD model exports the thermal and momentum profiles in the water tank while the EES model simulates the vapor compression cycle. The EES system model outputs the heat flux profile as a boundary condition of coil segments in the CFD model. Therefore, the EES system model and CFD tank model exchange the information via the tank wall. By iterating the data between EES system model and CFD model, the solutions from the two models can be matched. This method is proposed by Shah and Hrnjak [17] and refined by Li and Hrnjak [18]. Since the OCR is within 0.3% which is fairly small during the heating up process, the oil effect on the HPWH system performance is assumed to be neglected, the thermodynamic properties in the model is set to be those of the pure refrigerant.

8.2 Vapor Compression Cycle System Model Using EES

A quasi-steady-state EES system model is generated. The model contains three sub-systems to simulate and predict the thermal behavior of the condenser, evaporator and compressor. The Electronic Expansion Valve is set to be isenthalpic.

8.2.1 Compressor model

Two methods are used in this project for the calculation of compressor. Staley et al. [21] modeled the compressor by relating the compressor isentropic efficiency and volumetric efficiency to the compression ratio via the efficiency equations. The efficiencies are obtained by

linear curve fitting based on the experimental data. Then the compressor power and refrigerant mass flow rate can be calculated through the isentropic efficiency and volumetric efficiencies, according to the Equation (8.1) and (8.2):

$$W_{comp} = \frac{W_{is}}{\eta_{is}} \tag{8.1}$$

$$\dot{m}_{ref} = \eta_v \cdot \dot{V}_{disp} \cdot \rho_{suc} \tag{8.2}$$

In the equations, W_{is} is the isentropic work, η_{is} is the isentropic efficiency. η_v represents the volumetric efficiency while $\dot{V}_{disp}$ is the displacement rate and ρ_{suc} is the compressor suction density.

By using this compressor efficiency model, the compressor discharge temperature and pressure can thus be calculated iteratively.

Another method is to use AHRI 10-coefficient compressor maps in order to obtain refrigerant mass flow rate through the compressor and compressor power consumption. The performance map of a single-speed rotary compressor obtained from manufacturer is used in the compressor model. Equations (8.3) and (8.4) shown below are flow rate and power as functions of evaporation and condensation temperatures.

$$\dot{m} = \alpha_1 + \alpha_2 T_{evap} + \alpha_3 T_{cond} + \alpha_4 T_{evap}^2 + \alpha_5 T_{evap} T_{cond} + \alpha_6 T_{cond}^2 + \alpha_7 T_{evap}^3 + \alpha_8 T_{evap}^2 T_{cond} + \alpha_9 T_{cond}^2 T_{evap} + \alpha_{10} T_{cond}^3 \tag{8.3}$$

$$\dot{W} = \beta_1 + \beta_2 T_{evap} + \beta_3 T_{cond} + \beta_4 T_{evap}^2 + \beta_5 T_{evap} T_{cond} + \beta_6 T_{cond}^2 + \beta_7 T_{evap}^3 + \beta_8 T_{evap}^2 T_{cond} + \beta_9 T_{cond}^2 T_{evap} + \beta_{10} T_{cond}^3 \tag{8.4}$$

In the equations, T_{cond} is the discharge saturation temperature and T_{evap} is the suction saturation temperature of the compressor.

Actual suction state is considered here to correct the compressor map mass flow prediction by using Dabri and Rice [22] method.

$$\dot{m}_{actual} = \left[1 + F_{mass}\left(\frac{v_{ARI\text{-}map}}{v_{actual}} - 1\right)\right] m_{ref,ARI\text{-}map} \quad (8.5)$$

Where empirical correction factor $F_{mass} = 0.75$. $\frac{V_{ARI\text{-}map}}{V_{actual}}$ is the ratio of specific volume at compressor map to the specific volume at actual superheat. $\dot{m}_{actual}$ and $m_{ref,ARI\text{-}map}$ are the mass flow rates at compressor map and actual superheat.

For the alternative refrigerants such as R1234yf, it can be assumed that at the same suction and discharge pressures, the volumetric and isentropic efficiencies of the compressor remain the same. In consequence, the efficiencies can be decreased based on the original R134a maps as a function of the compressor inlet and outlet pressures. Equations (8.6) and (8.7) below define the volumetric and isentropic efficiencies.

$$\eta_v = \frac{\dot{m}}{V_{dis} \times rpm \times \rho_{suc}} \quad (8.6)$$

$$\eta_{is} = \frac{\dot{m} \times (h_{dis} - h_{suc})}{\dot{W}} \quad (8.7)$$

where η_v and η_{is} are the compressor volumetric and isentropic efficiencies, h_{dis} and h_{suc} are the enthalpies of compressor suction line and discharge line.

8.2.2 Heat Exchanger models

Since the inlet and outlet temperatures are not given, the LMTD-method becomes cumbersome to use. Therefore, the HPWH system model uses the finite element approach, by using a segment-to-segment method similar to [23,24], the single tube is divided into finite elements. Each tube element has refrigerant side and other side (air for evaporator, water for condenser) entering flow states, and phase changes are considered, therefore, the Effectiveness-Number of Transfer Unit (ε-NTU) method is used for heat transfer calculations between the refrigerant and air (water) side within each element.

The definition of heat exchanger effectiveness, ε, is the ratio between the actual heat transfer to the maximum possible heat transfer, which is shown in equation (8.8) as a dimensionless ranging between 0 and 1.

$$\varepsilon = \frac{Actual\ heat\ transfer}{Theoretical\ maximum\ heat\ transfer} = \frac{q_{act}}{q_{max}} \tag{8.8}$$

Where q_{max} is the maximum possible heat transfer for the heat exchanger. The maximum value could be obtained is one of the fluids undergo a temperature change that equal to the maximum temperature difference present in the heat exchanger, which is the difference in the inlet temperatures for hot and cold fluid.

$$q_{max} = C_{min}\ (T_{h,i}\text{-}T_{c,i}) \tag{8.9}$$

$$q_{act} = \varepsilon\ C_{min}\ (T_{h,i}\text{-}T_{c,i}) \tag{8.10}$$

The number of transfer unit (NTU) is used to represent the sensible heat transfer in heat exchanger.

$$NTU = \frac{UA}{C_{min}} \tag{8.11}$$

Where C_{min} is the minimum thermal capacity (the maximum temperature difference), UA is the overall heat transfer coefficient which can be obtained by

$$\frac{1}{UA} = \frac{1}{h_{hot}A_{hot}} + \frac{\delta}{kA_{hot/cold}} + \frac{1}{h_{cold}A_{cold}} \tag{8.12}$$

Where A is the contact area for each fluid side, k is the thermal conductivity of the wall, $h_{hot/cold}$ is the convective heat transfer coefficient for hot or cold stream, and δ represents the wall thickness.

Note that the term $\frac{\delta}{k}$ is the thermal resistance and $\frac{1}{h}$ represents the convective thermal resistance.

The effectiveness of the cross-flow heat exchanger of the HPWH system can be obtained and validated by using Navarro and Cabezas-Gomez [25] method

$$\varepsilon = 1 - \exp\{\left(\frac{1}{R}\right) \cdot NTU^{0.22} \cdot [\exp(-R \cdot NTU^{0.78}) - 1]\} \quad (8.13)$$

Where R is the heat capacity ratio

$$R = \frac{C_{min}}{C_{max}} \quad (8.14)$$

In the two-phase region, ${C_{min}}/{C_{max}} \to 0$ and all the heat exchanger effectiveness relations approach to the single equation,

$$\varepsilon = 1 - e^{-NTU} \quad (8.15)$$

Therefore, the heat transfer and outlet temperatures for one segment are obtained by using the above equations. Then the states and conditions at the outlet of the segment are able to be delivered to next segment as the inlet information.

8.2.3 Evaporator

The fin-and-tube evaporator is used in the Heat Pump Water Heater System. The table below shows some geometrical information.

Table 8.1 Evaporator geometry

Tube material	Cu	Inner tube diameter [mm]	0.432
Transverse tube spacing [m]	0.024	Outer tube diameter [mm]	0.343
Longitudinal tube spacing [m]	0.016	Evaporator width [m]	2
Fin density [m^{-1}]	630	Evaporator height [m]	13
Fin pitch [mm]	1.59	Circuits	7.9
Fin thickness [mm]	0.11	Passes per circuit	8.5

For a fin-and-tube evaporator, the effect of fin needs to be taken into consideration, therefore equation can be modified to

$$\frac{1}{UA} = \frac{1}{\eta_{fin} h_{hot} A_{hot}} + \frac{\delta}{k A_{hot/cold}} + \frac{1}{h_{cold} A_{cold}} \tag{8.16}$$

Where η_{fin} is the surface efficiency of the evaporator fins.

Air-side heat transfer coefficient h_{air} is obtained by using correlations from Wang et al. Equation presents the Coburn j-factor for a slit evaporator fin design

$$\mathrm{j} = 0.086 \cdot Re_{D_C}^{j_1} \left(\frac{F_p}{D_C}\right)^{j2} \left(\frac{F_p}{D_h}\right)^{j_3} \left(\frac{F_p}{P_t}\right)^{-0.93} N^{j_4} \tag{8.17}$$

And a-d shows the related coefficients

$$j_1 = -0.361 - \frac{0.042N}{\ln\left(Re_{D_C}\right)} + 0.158 \ln[N \left(\frac{F_p}{D_C}\right)^{0.41}] \tag{8.18}$$

$$j_2 = -0.083 + \frac{0.058\, N}{\ln\left(Re_{D_C}\right)} \tag{8.19}$$

$$j_3 = -5.735 + 1.211 \ln \left(\frac{Re_{D_C}}{N}\right) \tag{8.20}$$

$$j_4 = -1.224 - \frac{0.076 \left(\frac{j_1}{D_h}\right)^{1.42}}{\ln\left(Re_{D_C}\right)} \tag{8.21}$$

Where Re_{D_C} is the Reynolds number obtained by the tube collar diameter D_C, F_p is the evaporator fin pitch, D_h is the air flow hydraulic diameter, and N is the tube row number.

Therefore, equation presents the air side heat transfer coefficient

$$h_{air} = j \cdot G_{air} \cdot c_{p,air} \cdot Pr_{air}^{-0.667} \tag{8.22}$$

On the refrigerant side, to calculate the single-phase heat transfer coefficient, the correlation proposed by Gnielinski is used for turbulent flow heat transfer through circular tubes, which the effects of tube wall roughness can be taken into consideration.

$$h_{ref} = \frac{Nu_D \cdot D}{k_{ref}} \tag{8.23}$$

$$Nu_D = \frac{(f/8)(Re_D\text{-}1000)Pr}{1+12.7(f/8)^{1/2}(Pr^{2/3}\text{-}1)} \tag{8.24}$$

Where f denotes the Darcy friction factor, which can be obtained from Moody chart or for smooth tubes from Petukhov-Popov [26] correlation

$$f = (0.790\ lnRe_D\text{-}1.64)^{-2} \tag{8.25}$$

For the two-phase heat transfer coefficient, Wattelet et al. [27] proposed the asymptotic model considering two components that make up the two-phase heat transfer coefficient h_{tp}: nucleate boiling $h_{nb}$and convective boiling h_{cb}.

$$h_{tp} = [h_{nb}^n + h_{cb}^n]^{1/n} \tag{8.26}$$

Where the exponent n is considered to be 2.5. Nuclear boiling $h_{nb}$and convective boiling h_{cb} are calculated by the following correlations:

$$h_{nb} = 55q''^{0.67} W_m{}^{-0.5} Pr_{ref}^{0.12} [-\log_{10} Pr_{ref}]^{-0.55} \tag{8.27}$$

$$h_{cb} = F h_{liq} R \tag{8.28}$$

Where q'' is the heat flux, W_m is the refrigerant mole weight, Pr_{ref} is the Prandtl number of the refrigerant property. h_{liq}, F and R can be computed using following equations:

$$h_{liq} = 0.023 \frac{k_{ref,liq}}{D} Re_{liq}^{0.8} Pr_{liq}^{0.4} \tag{8.29}$$

$$\mathrm{F} = 1 + 1.925 X_{tt}^{-0.83} \tag{8.30}$$

$$\mathrm{R} = 1.32 Fr_{liq}^{0.2}, \text{ when } Fr_{liq} < 0.25 \tag{8.31}$$

$$\mathrm{R}=1, \text{ when } Fr_{liq} \geq 0.25 \tag{8.32}$$

Where the liquid Fraud number and Lockhart-Martinelli number can be calculated by:

$$Fr_{liq} = \frac{G_{ref}^2}{\rho_{ref,liq} g D} \tag{8.33}$$

$$X_{tt} = (\frac{1-x}{x})^{0.875} (\frac{\rho_v}{\rho_l})^{0.5} (\frac{\mu_l}{\mu_v})^{0.125} \tag{8.34}$$

The single-phase pressure drop is obtained by using the correlation of Churchill et. al [28] friction factor:

$$f_c = (\frac{1}{(A+B)^{3/2}})^{1/12} + \frac{8}{Re} \tag{8.35}$$

$$\mathrm{A} = [2.475(\frac{1}{(\frac{7}{Re})^{0.9} + \frac{0.27\varepsilon}{D}})]^{16} \tag{8.36}$$

$$\mathrm{B} = (\frac{37530}{Re})^{16} \tag{8.37}$$

This is the curve fitting for Moody's friction factor charts which can be applied for both laminar and turbulent regions in smooth and rough tubes, where ε is the tube surface roughness.

The two-phase pressure drop in a horizontal tube can be divided into two parts: Frictional pressure drop ΔP_f and acceleration pressure drop ΔP_a :

$$\Delta P_{tp} = \Delta P_f + \Delta P_a \tag{8.38}$$

To calculate the acceleration pressure drop ΔP_a, the following momentum balance can be applied:

$$\Delta P_a = G_{ref}^2 \left\{ \left[\frac{x_o^2}{\rho_v \alpha_o} + \frac{(1-x_o)^2}{\rho_l (1-\alpha_o)^2} \right] - \left[\frac{x_i^2}{\rho_v \alpha_i} + \frac{(1-x_i)^2}{\rho_l (1-\alpha_i)^2} \right] \right\} \tag{8.39}$$

Where α_i and α_o are the void fraction for the inlet and outlet respectively. This void fraction is calculated by using the correlation from Rouhani and Axelsson [29] :

$$\alpha = \frac{x}{\rho_v} \left\{ C \left[\frac{x}{\rho_v} + \frac{1-x}{\rho_l} \right] + \frac{1.18}{G_{ref}} [\frac{\sigma_{ref} g (\rho_l - \rho_v)}{\rho_l^2}]^{0.25} \right\}^{-1} \tag{8.40}$$

Where σ_{ref} is the refrigerant surface tension, and C can be obtained by:

$$C = 1 + 0.2(1 - x) \tag{8.41}$$

To calculate the frictional pressure drop for the two-phase refrigerant flow, a correlation proposed by Muller et al. [30] can be used based on the flow quality:

$$\left(\frac{\partial P}{\partial z}\right)_g = f_g \frac{G_{ref}^2}{2\rho_g D_h} \tag{8.42}$$

The frictional gradient of total refrigerant liquid flow can be obtained by:

$$\left(\frac{\partial P}{\partial z}\right)_{lo} = G_{ref}(1 - x)^{1/3} + \left(\frac{\partial P}{\partial z}\right)_g x^3 \tag{8.43}$$

f_g is the single phase (vapor) Darcy friction factor where:

$$f_g = \frac{64}{Re_g} \text{ for } Re_g \leq 1187 \tag{8.44}$$

$$f_g = \frac{0.3164}{Re_g^{0.25}} \text{ for } Re_g > 1187 \tag{8.45}$$

8.2.4 Condenser model

This HPWH unit contains a wrapped around coil condenser. Two parallel circuits of tube coils are wrapped around the water tank wall. Each circuit contains 16 coils and the refrigerant flow inside the coils is going upward. Therefore, the superheated refrigerant from compressor enters from the tank top to the bottommost coil, then two-phase refrigerant goes upward in the condenser and the subcooled refrigerant exits the condenser from the top.

In order to simplify the modelling process, it is assumed that the two condenser circuits split the refrigerant entering the condenser and there is no maldistribution, so the two circuits have identical states of refrigerant. Therefore, in the model, these two circuits are simplified as one circuit which contains doubled contact area with tank wall as well as doubled cross-sectional area.

Figure 8.1 shows that the condenser contains N coils in the Finite Volume Method, and to simplify the model, each coil is wrapped around the tank horizontally without any slopes. Furthermore, in order to realize the interaction between the tank and coil, the model uses a segment-to-segment method that each coil has been divided into M elements, as it shown in Figure 8.2.

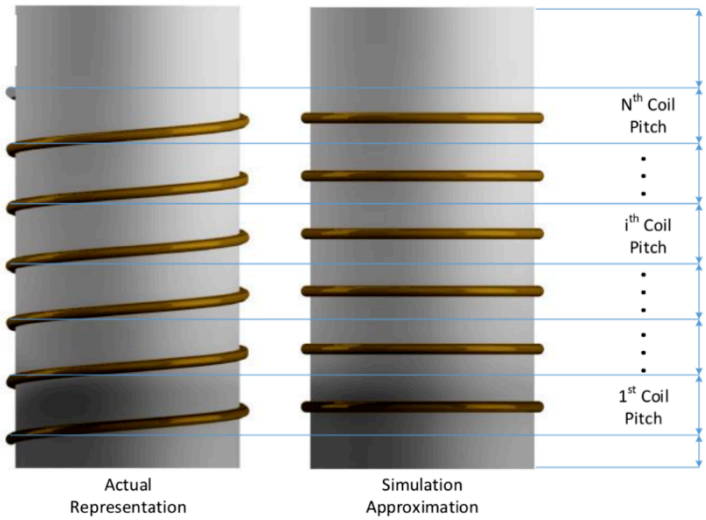

Figure 8.1 Adaptation of coils windings in modelling

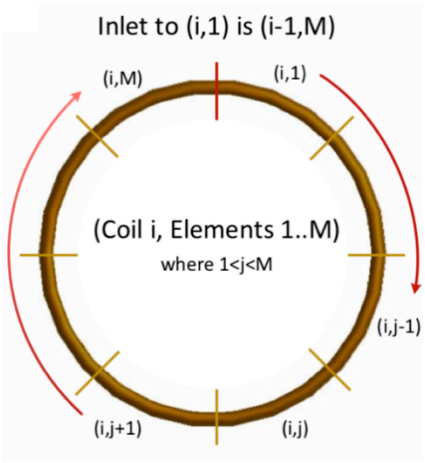

Figure 8.2 Discretization of each coil into elements

Since each coil has been discretized into M elements, Figure 8.3 shows the simulation of each element. Each segment of the condenser coil tube is assigned to its specific geometrical location (i,j) in the water tank. Therefore, the heat transfer and pressure drop can be calculated along the refrigerant upward flow. Each single coil segment has its own corresponding segment of tank wall and water segment, these three segments compose the area for refrigerant side heat transfer, the thermal resistance from the tube to the tank wall thickness, and the natural convection heat transfer between water element and tank wall.

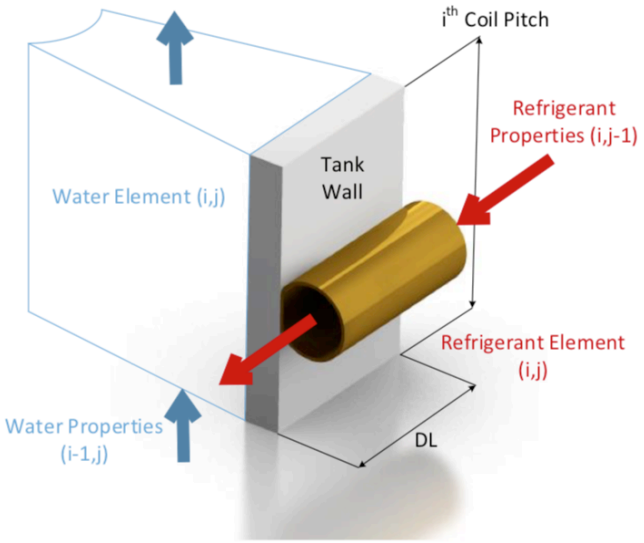

Figure 8.3 Single element of condenser

Figure 8.4 shows the model reduction of the refrigerant coils and tank wall. The coil tubes and tank walls are simplified to fins and the arrow indicates the heat transfer direction. This heat transfer is driven by the temperature difference between the refrigerant segment and water element corresponding to that refrigerant segment.

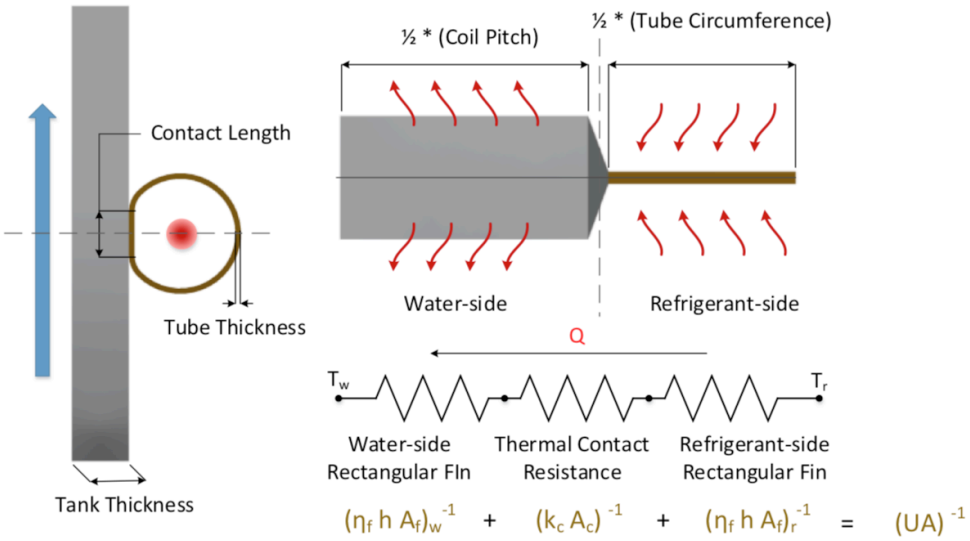

Figure 8.4 Simplification of element level modelling and description of heat path

On the refrigerant side, same correlations used in the evaporator are chosen to calculate the single-phase heat transfer and pressure drop in the condenser. For the two-phase heat transfer

correlation, Xiao and Hrnjak's model [31,32] is applied. In their model, the superficial quality for the void fraction is introduced to account for the non-equilibrium effects of the tube condensation.

On the water side, the heat transfer coefficient is calculated by using the heat transfer correlation based on the external laminar flow through a flat plate.

$$\mathrm{Nu} = 0.664 Re^{1/2} Pr^{1/3} \tag{8.46}$$

where the characteristic length is the thickness of the upward flow layer which will be discussed later.

8.3 Water Side CFD Model

The temperature and velocity profiles in the water tank are simulated by using the CFD model in ANSYS Fluent. This CFD model is designed as a Two-Dimensional axisymmetric domain that simulates the heating process of the water tank, as it shown in Figure 8.6. One axisymmetric boundary represents the centerline of the water tank, and the other three boundaries corresponds to the tank walls including the top, bottom and side wall.

Due to the buoyancy effect, the water nearby the tank wall flows in an upward direction and is heated by the tank wall conduction. An "upward flow layer" is then defined to account for the upward flow velocity component in the nearby wall area, as it shown in Figure 8.5. The water flows downward outside the upward flow layer area due to the circulation. According to the CFD model simulation, this layer is set to be 1 cm.

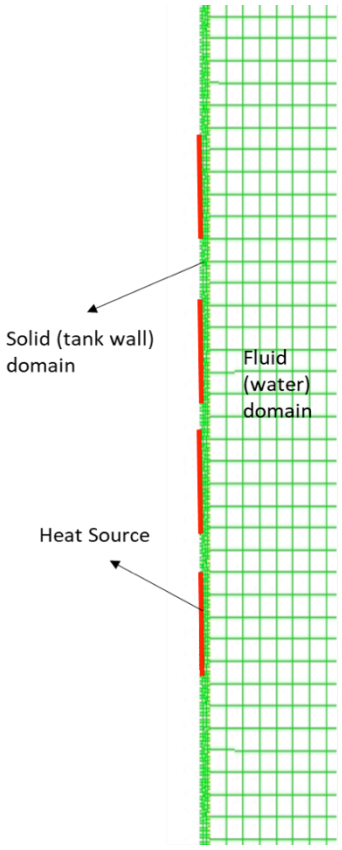

Figure 8.5 Zoom in the near-wall area

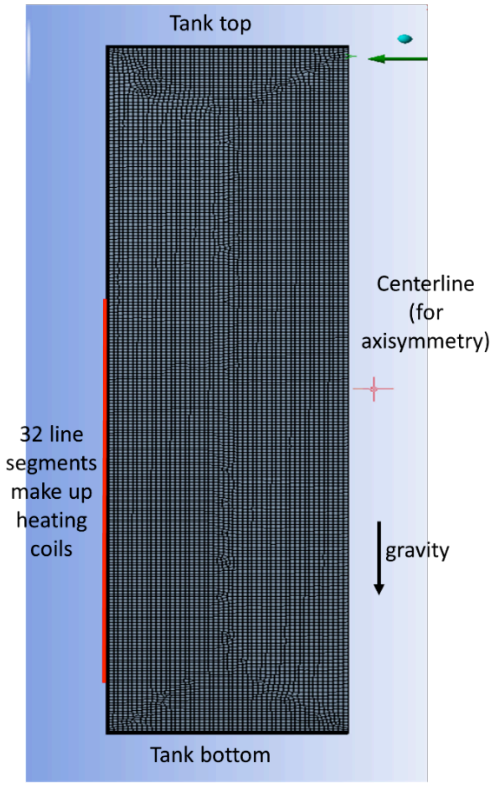

Figure 8.6 Geometry and mesh of the water tank CFD model

54280 cells are used in the CFD quadrangular mesh to better obtain the thermal and momentum profiles between the water side and tank wall, and the refinement has been used to intensify the grid density near the upward flow layer.

As it shown in Figure 8.5, each line segment represents one of the 16 condenser coils, the length of each segment equivalents to the coil pitch. The heat flux is assumed to be uniform on each segment's surface and it is specified by the User Defined Function file that obtained from the quasi-steady-state vapor compression system model.

It is assumed that the density of the tank water has a linear relation with the temperature, and the buoyancy driven flow is set to be laminar flow. Based on the assumptions that made before, governing equations are solved by using Finite Volume Method and pressure based solver.

SIMPLE (semi-implicit method for pressure-linked equations) scheme has been applied to pressure-velocity coupling, Green-Gauss Node Based has been chosen as the gradient, and Second Order scheme is used for the pressure accuracy. To improve the accuracy, Second Order Upwind has been applied for momentum and energy. The convergence standard has been taken as 1e-06 for the pressure residual, and for the continuity residual, 1e-3 has been selected.

8.4 EES-CFD Linked model

The CFD model outputs the near-wall water temperature and velocity of each segment coil to the EES system model for heat transfer calculation. The EES system model outputs the heat flux profile as a boundary condition of coil segments in the CFD model. Therefore, the EES system model and CFD tank model exchange the information via the tank wall. By iterating the data between EES system model and CFD model, the system performance solutions from two models can be matched.

Figure 8.7 illustrates the flow diagram of the linked model algorithm. First, the iteration begins with a guessed value of coil segment heat flux. With the heat flux profile in UDF, the CFD model simulates the first heating-up process. After that, CFD model outputs the near-wall water temperature and velocity profiles to the EES system model, then, the system model generates a new heat flux profile for CFD model for next simulation. This linked model runs iteratively and exchanges the profile internally until the heat flux becomes stable (change within 1% variation).

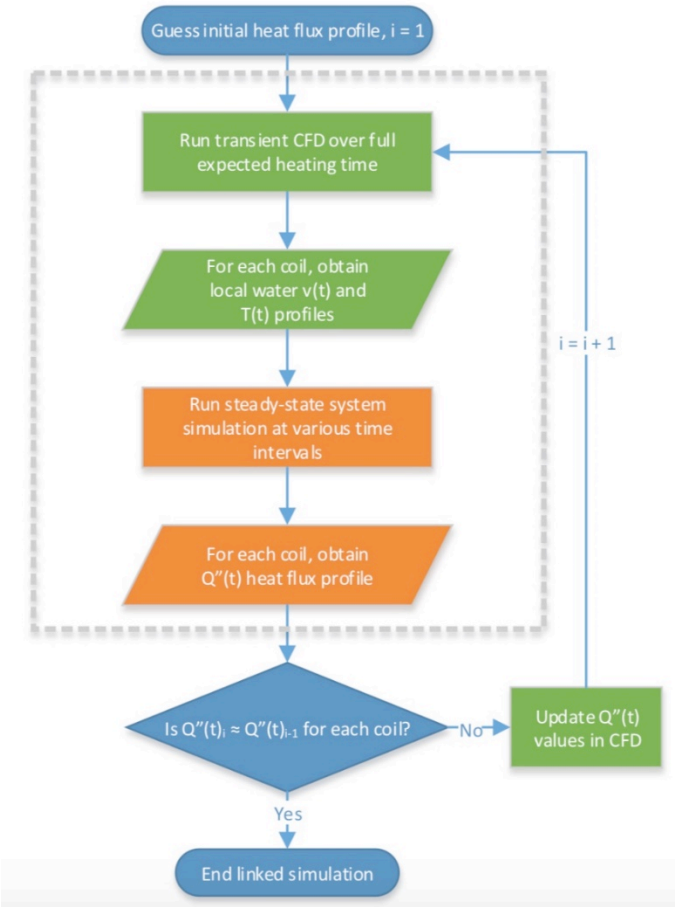

Figure 8.7 Linked algorithm between EES and CFD model

8.5 Modelling Results

The temperature contours and velocity trajectories at 60 min, 120 min and 180 min are given in Figure 8.8 and 8.9. Combining the two figures, it can be observed that the upward flow is restricted in a thin layer that near the tank wall. The water flows upward while the outside water flows downward, the water temperature in that layer is also higher than the outside water temperature. From the three charts in Figure 8.9, it is shown that the flow patterns at different time point remain relatively similar, only velocity magnitude changes slightly with time. However, for the three charts in Figure 8.8, there is a significant difference among temperature contours at different time. The thermal stratification is getting intensive and obvious with time

that a thicker thermocline is achieved with longer heating time. The temperature difference between the tank top and bottom is over 20 ℃ at 180 mins that the Boussinesq approximation may not be applicable to that high temperature difference.

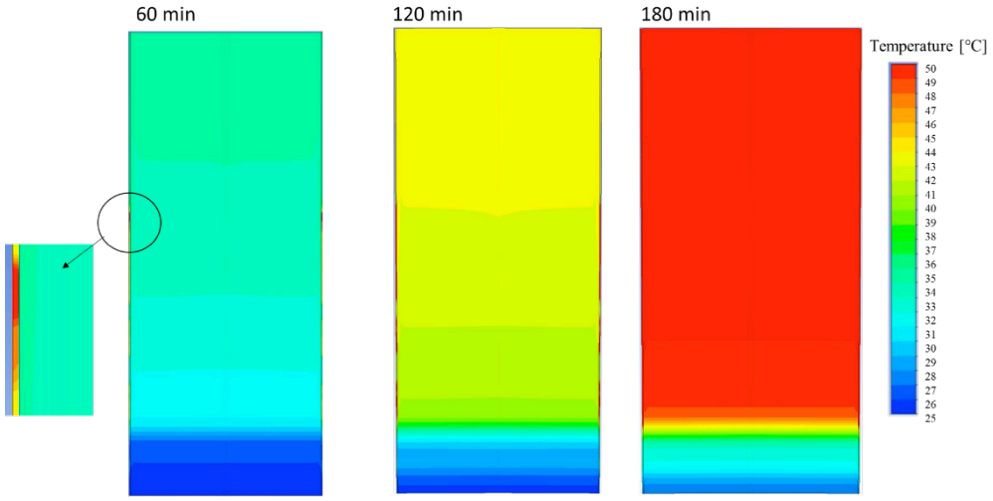

Figure 8.8 Temperature contours at t = 60 min, t = 120 min and t= 180 min

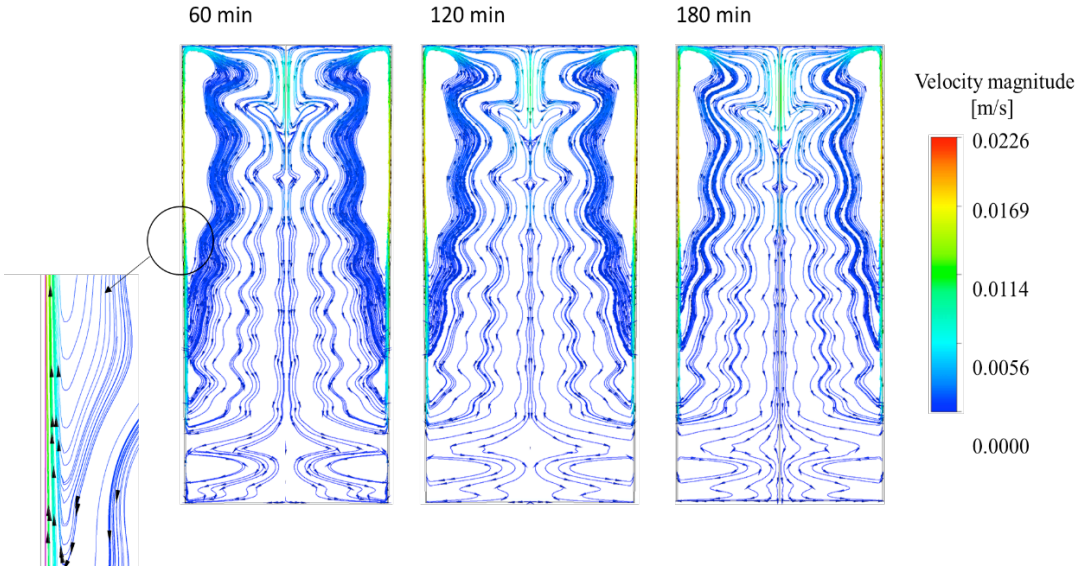

Figure 8.9 Velocity trajectories at t = 60 min, t = 120 min and t= 180 min

The importance of the upward flow layer for analyzing the system has been mentioned above. For a better insight of the interaction between the vapor compression system and the water tank,

Figure 8.10 and 8.11 plot the average temperature and velocity profile at each corresponding coil segment in the upward flow layer, at several heating-up times.

From Figure 8.10, it is proved again that the stratification becomes more intensive as the heating time goes longer. Furthermore, the temperature in the upward flow layer is 0.5℃ - 2.5℃ higher than the tank centerline temperature. From Figure 8.11, the velocity profiles at different time have quite similar trend, this coincides well with the velocity trajectories that the water flow in the tank is stable during the heating up process.

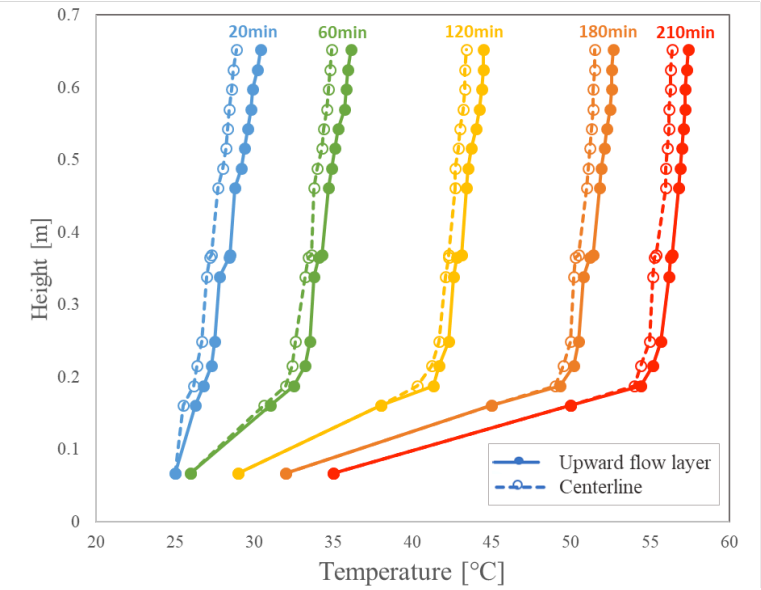

Figure 8.10 Temperatures in the upward flow layer is 0.5℃ - 2.5℃ higher than the tank centerline temperature

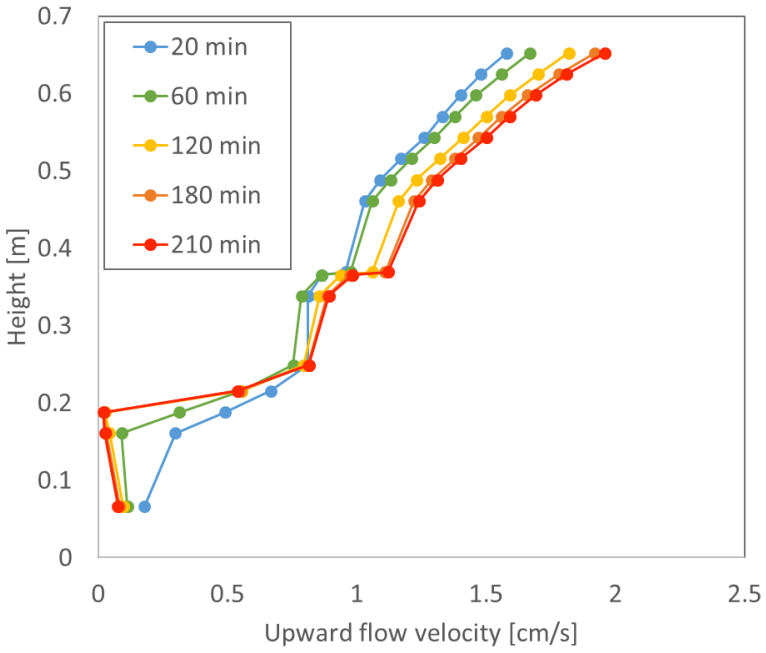

Figure 8.11 Upward flow layer velocity decreases with time at lower coil level and increases with time at upper coil level

Furthermore, the near-wall velocities at different heating time show similar trends and increase with the coil height. The velocity decreases with time at first three coils from the bottom, and increases with time at upper coil level.

The linked model is able to capture the thermal behavior of the water in the tank. As it has been described before, three series of thermocouples are placed at three different location inside the tank to record the temperature change during the heating-up process. Therefore, the temperatures at each corresponding thermocouple location are obtained from CFD model to validate the experimental temperature profiles. The average temperature of the tank domain is compared with the vertical thermocouple series, and two horizontal series are compared with the average temperature at the corresponding heights in the tank model. The comparison between the CFD model and experimental data is shown in Figure 8.12.

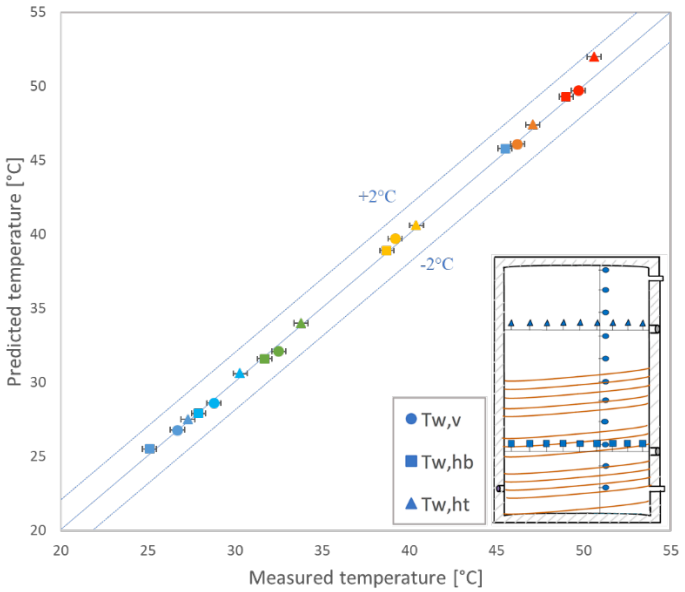

Figure 8.12 The predicted water temperatures match the experimental data, the deviations are within 2°C.

Figure 8.12 indicates that the predicted water temperatures match the experimental within a deviation of 2°C. Therefore, the CFD model can be used to predict the thermal and momentum changes in a transient heating up process.

The model validation of the capacities of condenser and evaporator, the compressor work and COP is given in Figure 8.13. It shows that the system model predictions coincide well with the experimental data. The prediction of COP matches the experimental COP fairly well that the deviation is within 4.5% while the average deviation is 1.0%. The average deviation of condenser capacity and compressor work is 0.79%. However, the average deviation of the evaporator capacity is 12.5%, and this might due to some imperfections in manufacturing which are not considered in the system model.

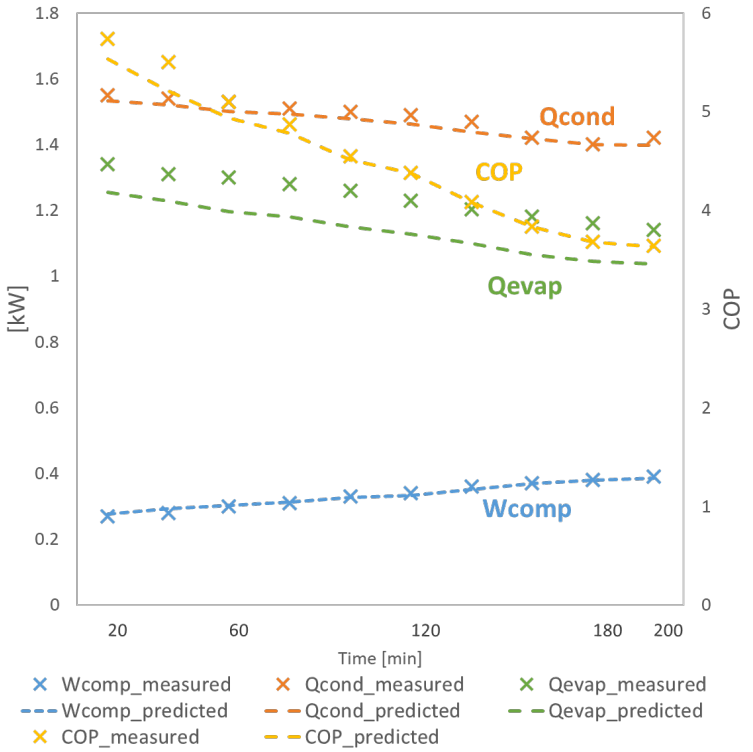

Figure 8.13 The predictions of the heat exchangers' capacities, compressor work and COP matches well with the experimental data.

Figure 8.14 gives the comparison between the experimental data and measurements of the refrigerant at the inlet and outlet of the evaporator. It shows that the prediction deviations of refrigerant temperatures at the inlet and outlet of the evaporator are within 0.5℃.

The comparison between the experimental data and model predictions of the refrigerant at the inlet and outlet of the condenser is shown in Figure 8.15. The prediction deviation is within 2℃ and it could be found that most of the predictions are within 0.5℃.

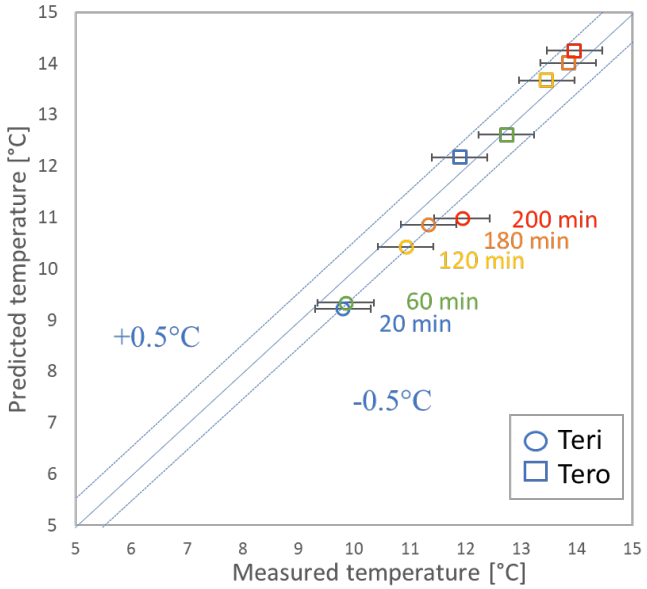

Figure 8.14 The prediction deviations of refrigerant temperature at the inlet and outlet of the evaporator are within 0.5℃.

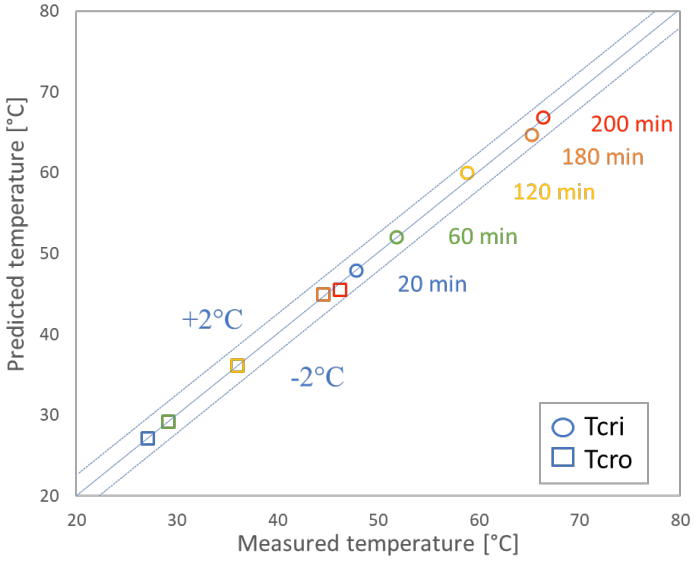

Figure 8.15 The prediction deviations of refrigerant temperature at the inlet and outlet of the evaporator are within 2℃.

Figure 8.16 presents the comparison between the measured and predicted results of the refrigerant flow pressure drop in the condenser and evaporator. It shows that the model can properly predict the condenser pressure drop within ±10% deviation. However, the model

underestimates the refrigerant pressure drop on evaporator, the predicted results are much smaller than experimental data. This additional pressure drop may due to the brazed joints at the end of each horizontal tubes. It could also be explained by the U-bend effect on the flow regime. In the model the friction factor is determined with the pressure drop in the U-bend region being neglected. Besides, the imperfectness in manufacturing would also cause the pressure drop, which is not considered in the modelling.

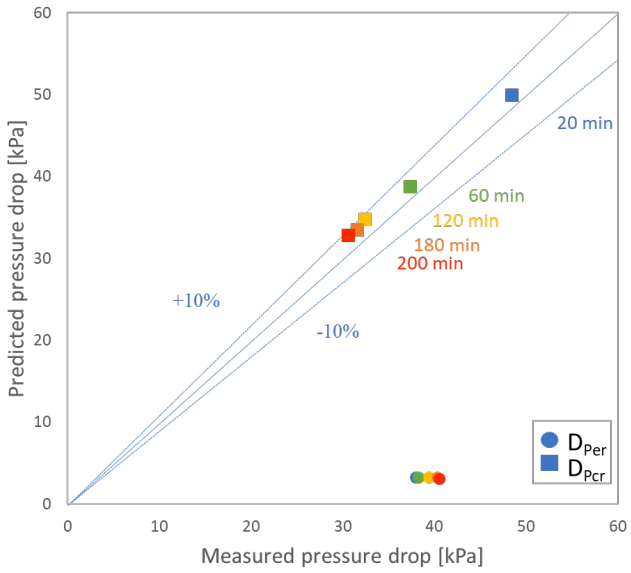

Figure 8.16 Model predicts the refrigerant pressure drop in the condenser within ±10% deviation, but underestimates the refrigerant pressure drop on evaporator.

CHAPTER 9-SUMMARY AND CONCLUSIONS

9.1 Conclusions from Experimental Study on Water Side

In conclusion, the warm-up and recovery performances of a residential Heat Pump Water Heater have been investigated. The conclusions of the experimental results are summarized as follows:

- For constant draw rate, draw amount does not affect system efficiency (COP) significantly. Only 3% of performance difference exists with the increase of draw amount from 50% of the tank capacity to 100%.
- For constant draw amount, higher draw rate reduces efficiency. Higher draw rate results in higher mixing, thus condensation temperature increases and the recovery efficiency (COP) drops.

  Higher draw rate results in more mixing. Entropy, Richardson Number and Mixing Coefficient are introduced to characterize the stratification level of the thermal storage tank. Less entropy generation, higher Richardson Number and lower Mixing Coefficient indicate a better stratified thermal tank.
- 3D CFD simulation is introduced to describe and explore the thermal tank numerically. The results from experiments for effect of draw rate on stratification agrees with the CFD results.

  Entrance effect has also been explored on stratification. A tank with higher inlet position obtains greater mixing. Baffles and nozzles can be used as effective tools to reduce mixing in the thermal tank.

9.2 Conclusions from Experimental Study on Refrigerant Side

Series of experiments in the heating-up process of a Heat Pump Water Heater have been conducted. The following conclusions are drawn for each experiment:

- A drop-in analysis of R1234yf is carried out to compare the system performance with R134a on the same experimental facility at the same working condition. R1234yf can be considered as a drop-in refrigerant to R134a system without any special changes in the heat pump facility.
  (a) R1234yf introduces COP decreases ranging between 5.8% and 9.7%.
  (b) The power consumption of R1234yf is 1.3% higher than that of R134a.
  (c) The heating capacity of R1234yf is up to 10% lower than that of R134a.
  (d) Refrigerant charge amount of R1234yf is 5% lower than that of R134a.
- A simple modification has been made for the HPWH system by closing one condenser circuit. R134a and R1234yf are separately used to compare the performance with one circuit and with two circuits.
  (a) Compared with the system with two-circuit original condenser, COPof the system with one-circuit condenser obtains a reduction of 3.7% using R134a and 5.5% using R1234yf.
  (b) Cooling capacity for the system with one-circuit condenser decreases by 0.2%-4.1% for R134a, and decreases up to 0.7% for R1234yf.
  (c) Heating capacity for the system with one-circuit condenser decreases by 0.1%-4.3% for R134a, and has an average increment of 0.5% for R1234yf.
  (d) The charge amount of the system with one-circuit condenser decreases 25% for both refrigerant.

9.3 Conclusions from System Performance Model

A linked EES-CFD model has been developed to simulate the transient warm-up period of a Heat Pump Water Heater. The CFD model describes the heat transfer and fluid dynamics on the water side, while EES system model describes a vapor compression cycle. The conclusions of the system performance modelling are summarized as below:

- The linked EES-CFD model is found to be in good agreement with experimental results conducted in the same heating up activity, and it is capable of predicting the temperature distribution of the vapor compression system and transient behaviors of the thermal storage tank. The deviations of the refrigerant temperatures in two heat exchangers and water temperature in the storage tank are within 2℃, and the model predicts the system power and capacities within the average deviation of 4.1%.
- The predicted pressure drop in condenser is within 10% deviation, however, the model underestimates the pressure drop in evaporator due to the local pressure loss due to defects from manufacturing which is not counted in the system model.

REFERENCE

[1] U. Jordan, S. Furbo. Thermal stratification in small solar domestic storage tanks caused by draw-offs, *Solar Energy*, 78, 291–300, 2005.

[2] C. Yee, F. Lai. Effects of a porous manifold on thermal stratification in a liquid storage tank, *Solar Energy*, 71, 241–254, 2001.

[3] J. Dragsted, S. Furbo, M. Dannemand, F. Bava, Thermal stratification built up in hot water tank with different inlet stratifiers. *Solar Energy*, 147, 414–425, 2017.

[4] J. H. Davidson, D.A. Adams, J.A, Miller. A coefficient to characterize mixing in solar water storage tanks, *Transactions of the ASME, Journal of Solar Energy Engineering* 116, 94–99, 1994.

[5] M. A. Rosen, R. Tang, I. Dincer. Effect of stratification on energy and exergy capacities in thermal storage systems, *International Journal of Energy Research*, 28, 177-193, 2004.

[6] M. Y. Haller, E. Yazdanshenas, E. Andersen, C. Bales, W. Streicher, S. Furbo. A method to determine stratification efficiency of thermal energy storage processes independently from storage heat losses, *Solar Energy*, 84, 997-107, 2010.

[7] A. Castell, M. Medrano, C. Sole, L. Cabeza. Dimensionless numbers used to characterize stratification in water tanks for discharging at low flow rates, Renewable Energy, 35, 2192-2199, 2010.

[8] Y. Lee, D. Jung. A brief performance comparison of R1234yf and R134a in a bench tester for automobile applications, *Applied Thermal Engineering*, 35, 240-242, 2012.

[9] C. Zilio, J. S. Brown, G. Schiochet, A. Cavallini. The refrigerant R1234yf in air conditioning systems, *Energy*, 36, 6110-6120, 2011.

[10] A. Mota-Babiloni, J. Navarro-Esbrí, Á. Barragán, F. Molés, B. Peris. Drop-in energy performance evaluation of R1234yf and R1234ze(E) in a vapor compression system as R134a replacements, *Applied Thermal Engineering*, 71, 259–265, 2014

[11]] J. Navarro-Esbrí, F. Molés, Á. Barragán-Cervera. Experimental analysis of the internal heat exchanger influence on a vapour compression system performance working with R1234yf as a drop-in replacement for R134a, *Applied Thermal Engineering*, 59, 153–161, 2013.

[12] H. Cho, H. Lee, C. Park. Performance characteristics of an automobile air conditioning system with internal heat exchanger using refrigerant R1234yf, *Applied Thermal Engineering*, 61, 563–569, 2013.

[13] Y. Lee, D.G. Kang, D. Jung. Performance of virtually non-flammable azeotropic HFO1234yf/HFC134a mixture for HFC134a applications, *International Journal of Refrigeration,* 36, 1203–1207, 2013.

[14] J. Li, P. Hrnjak. An Experimentally Validated Model for Microchannel Condensers with Separation Circuiting, International Refrigeration and Air Conditioning Conference at Purdue, Paper 2658, 2018.

[15] B. Baeten, T. Confrey, S. Pecceu, F. Rogiers, L. Helsen. A validated model for mixing and buoyancy in stratified hot water storage tanks for use in building energy simulations, *Applied Energy*, 172, 217-229, 2016.

[16] J. Fan, F. Simon, Y. Hongqiang. Development of a hot water tank simulation program with improved prediction of thermal stratification in the tank, *Energy Procedia*, 70, 193-202, 2015.

[17] T. Shah, P. Hrnjak. Linked modelling of heat pump water heater vapor compression system and water tank. *International Refrigeration and Air Conditioning Conference at Purdue*, Paper 1481, 2014.

[18] W. Li, P. Hrnjak. Experimentally validated model of heat pump water heater in heating-up transients. *International Journal of Refrigeration*, 88, 420-431, 2018.

[19] M. Y. Haller, E. Yazdanshenas, E. Andersen, C. Bales, W. Streicher and S. Furbo. A method to determine stratification efficiency of thermal energy storage processes independently from storage heat loss. *Solar Energy*, Vol. 84, No. 6, 997-1007, 2010.

[20] J. E. B. Nelson, A.R. Balakrishnan and S. Srinivasa Murthy. Experiments on stratified chilled-water tanks. *International Journal of Refrigeration*, 22, 216-234, 1999.

[21] D. M. Staley, C. W. Bullard, and R. R. Crawford, Steady-State Performance of a Domestic Refrigerator/Freezer Using R12 and R134a, *Technical Report ACRC TR-022*, University of Illinois at Urbana-Champaign, 1992.

[22] A. E. Dabiri, C. K. Rice. A compressor simulation model with corrections for the level of suction gas superheat. *ASHRAE Trans,* 87(2), 771-782, 1981.

[23] J. Li, and P. Hrnjak. The Analysis of Phase Separation in Vertical Headers of Microchannel HEs. No. 2016-01-0253. *SAE Technical Paper*, 2016.

[24] J. Li, P. Hrnjak. Separation of Liquid and Vapor in Header of MCHE. *International Refrigeration and Air Conditioning Conference at Purdue*, Paper 2248, 2016.

[25] H. A. Navarro, L. C. Cabezas-Gómez. Effectiveness-ntu Computation with a Mathematical Model For Cross-Flow Heat Exchangers. *Brazilian Journal of Chemical Engineering*, 24(4), 1678-4383, 2007.

[26] B. Petukhov, V. Popov. Theoretical calculations of heat exchange and frictional resistance in turbulent flow in tubes of an incompressible fluid with variable physical properties. *High Temp*, 1, 69-83, 1963.

[27] J. P. Wattlet, J. C. Chato, B. R. Christoffersen, et al. Heat transfer flow regimes of refrigerants in a horizontal-tube evaporator. *Technical Report ACRC TR-055*, University of Illinois at Urbana-Champaign, 1994.

[28] S. W. Churchill. Friction-factor equation spans all fluid flow regimes, *Chemical Engineering*, No. 7, pp.91-92, 1977.

[29] S.Z. Rouhani and E. Axelsson. Calculation of void volume fraction in the sub cooled and quality boiling regions. International Journal of Heat and Mass Transfer, 13, 383–393, 1970.

[30] Muller-Steinhagen. A Simple Friction Pressure Drop Correlation for Two-phase Flow in Pipes. *Chemical Engineering and Processing*, 20(6), 297-308, 1986.

[31] J. Xiao, P. Hrnjak. A new flow regime map and void fraction model based on the flow characterization of condensation. *International Journal of Heat and Mass Transfer*, 108, 443-452, 2017a.

[32] J. Xiao, P. Hrnjak. A heat transfer model for condensation accounting for non-equilibrium effects. International Journal of Heat and Mass Transfer, 111, 201-210, 2017b.

APPENDIX A: ORIGINAL DATA

Table A-1 two-circuit condenser with R134a

Time [min]	Qcond [kW]	Qevap [kW]	Wcomp [kW]	COP	Ter_o [°C]	Tcr_o [°C]	m [g/s]
5.00	1.53	1.47	0.26	5.91	16.97	28.65	8.43
10.00	1.50	1.37	0.26	5.68	10.07	28.75	8.15
15.00	1.53	1.41	0.27	5.70	12.51	27.68	8.19
20.00	1.54	1.40	0.27	5.62	12.77	27.36	8.12
25.00	1.56	1.41	0.28	5.65	12.71	27.37	8.18
30.00	1.56	1.39	0.28	5.56	12.30	27.46	8.10
35.00	1.56	1.40	0.28	5.52	13.00	27.74	8.11
40.00	1.53	1.37	0.29	5.32	12.94	28.04	7.96
45.00	1.53	1.37	0.29	5.27	13.68	28.29	7.97
50.00	1.56	1.39	0.29	5.33	13.88	28.60	8.11
55.00	1.54	1.36	0.30	5.21	13.53	29.04	8.00
60.00	1.52	1.35	0.30	5.09	13.75	29.50	7.95
65.00	1.52	1.35	0.30	5.05	13.17	30.05	7.99
70.00	1.54	1.36	0.31	5.06	12.68	30.54	8.12
75.00	1.52	1.33	0.31	4.91	12.35	31.10	8.00
80.00	1.52	1.34	0.31	4.87	12.99	31.85	8.05
85.00	1.52	1.34	0.32	4.82	12.62	32.44	8.12
90.00	1.51	1.33	0.32	4.78	12.93	33.10	8.08
95.00	1.50	1.31	0.32	4.64	12.55	33.81	8.06
100.00	1.50	1.31	0.32	4.64	13.01	34.49	8.11
105.00	1.48	1.30	0.33	4.50	13.77	35.21	8.03
110.00	1.51	1.32	0.33	4.57	13.22	36.02	8.25
115.00	1.51	1.31	0.33	4.52	12.66	36.84	8.26
120.00	1.48	1.29	0.34	4.37	12.89	37.50	8.17
125.00	1.49	1.30	0.34	4.36	13.52	38.15	8.27
130.00	1.47	1.27	0.34	4.27	13.09	38.86	8.18
135.00	1.45	1.28	0.35	4.22	15.83	39.23	8.12
140.00	1.49	1.28	0.35	4.25	11.94	40.02	8.36
145.00	1.43	1.24	0.36	4.02	13.76	40.99	8.09
150.00	1.46	1.28	0.36	4.10	15.70	41.26	8.27
155.00	1.47	1.27	0.36	4.07	13.81	42.03	8.38
160.00	1.42	1.23	0.36	3.91	14.89	42.88	8.15

Table A-1 (cont.)

165.00	1.43	1.25	0.37	3.90	16.70	43.16	8.21
170.00	1.46	1.26	0.37	3.94	15.13	43.95	8.45
175.00	1.44	1.22	0.38	3.84	11.28	45.02	8.41
180.00	1.42	1.23	0.38	3.75	15.41	45.61	8.32
185.00	1.41	1.21	0.38	3.68	14.99	46.29	8.28
190.00	1.39	1.19	0.39	3.59	13.78	47.08	8.28
195.00	1.40	1.21	0.39	3.60	16.02	47.61	8.33
200.00	1.40	1.18	0.40	3.53	12.61	48.48	8.42
208.00	1.39	1.15	0.40	3.47	10.47	49.02	8.38

Table A-2 two-circuit condenser with R1234yf

Time [min]	Qcond [kW]	Qevap [kW]	Wcomp [kW]	COP	Ter_o [°C]	Tcr_o [°C]	m [g/s]
5.00	0.04	0.04	0.26	0.14	18.07	26.54	8.43
10.00	1.30	1.21	0.28	4.73	16.47	27.27	8.15
15.00	1.39	1.25	0.28	4.96	15.63	27.91	8.19
20.00	1.41	1.25	0.29	4.96	15.15	28.51	8.12
25.00	1.43	1.25	0.29	5.01	14.90	29.15	8.18
30.00	1.42	1.24	0.29	4.92	14.70	29.64	8.10
35.00	1.42	1.24	0.29	4.87	14.61	30.32	8.11
40.00	1.41	1.22	0.29	4.79	14.61	31.00	7.96
45.00	1.38	1.21	0.30	4.66	14.49	31.52	7.97
50.00	1.40	1.22	0.30	4.70	14.61	32.17	8.11
55.00	1.38	1.20	0.30	4.59	14.59	32.77	8.00
60.00	1.36	1.18	0.30	4.45	14.58	33.32	7.95
65.00	1.37	1.18	0.31	4.45	14.68	34.11	7.99
70.00	1.34	1.16	0.31	4.33	14.79	34.63	8.12
75.00	1.34	1.15	0.31	4.29	14.80	35.09	8.00
80.00	1.34	1.15	0.31	4.27	14.92	35.69	8.05
85.00	1.33	1.15	0.32	4.22	15.02	36.16	8.12
90.00	1.32	1.14	0.32	4.16	15.09	36.82	8.08
95.00	1.33	1.14	0.32	4.15	15.16	37.16	8.06
100.00	1.30	1.12	0.32	4.05	15.21	37.70	8.11
105.00	1.29	1.11	0.32	4.00	15.24	38.41	8.03
110.00	1.28	1.09	0.33	3.92	15.39	39.32	8.25
115.00	1.29	1.10	0.33	3.94	15.50	39.52	8.26
120.00	1.28	1.09	0.33	3.88	15.54	40.12	8.17
125.00	1.26	1.07	0.33	3.77	15.57	40.83	8.27

Table A-2 (cont.)

130.00	1.25	1.06	0.34	3.71	15.68	41.25	8.18
135.00	1.26	1.06	0.34	3.74	15.66	41.61	8.12
140.00	1.24	1.05	0.34	3.65	15.76	42.21	8.36
145.00	1.24	1.04	0.34	3.62	15.84	42.87	8.09
150.00	1.23	1.03	0.34	3.59	15.89	43.34	8.27
155.00	1.24	1.05	0.35	3.60	16.00	43.73	8.38
160.00	1.21	1.02	0.35	3.49	15.99	44.67	8.15
165.00	1.21	1.02	0.35	3.44	16.07	44.75	8.21
170.00	1.23	1.03	0.35	3.49	16.09	45.42	8.45
175.00	1.22	1.02	0.35	3.44	16.19	46.15	8.41
180.00	1.23	1.02	0.36	3.42	16.23	46.42	8.32
185.00	1.23	1.02	0.36	3.41	16.30	46.95	8.28
190.00	1.20	1.00	0.36	3.32	16.35	47.46	8.28
195.00	1.20	1.00	0.37	3.29	16.46	48.09	8.33
200.00	1.21	1.00	0.37	3.29	16.47	48.14	8.42
205.00	1.18	0.98	0.37	3.18	16.54	49.11	8.25
210.00	1.19	0.98	0.37	3.21	16.60	49.34	8.26
215.00	1.20	0.99	0.38	3.20	16.63	49.94	8.17
220.00	1.17	0.97	0.38	3.12	16.65	49.99	8.27
225.00	1.17	0.97	0.38	3.10	16.73	50.89	8.18

Table A-3 one-circuit condenser with R134a

Time [min]	Qcond [kW]	Qevap [kW]	Wcomp [kW]	COP	Ter_o [°C]	Tcr_o [°C]	m [g/s]
5.00	1.23	1.24	0.25	4.96	24.05	27.20	6.57
10.00	1.42	1.38	0.28	5.09	20.16	26.66	7.70
15.00	1.59	1.45	0.29	5.57	14.20	27.89	8.40
20.00	1.58	1.41	0.29	5.46	11.14	28.11	8.29
25.00	1.61	1.41	0.29	5.53	11.04	28.45	8.35
30.00	1.60	1.41	0.29	5.46	11.59	28.76	8.20
35.00	1.60	1.40	0.29	5.41	10.75	29.06	8.35
40.00	1.59	1.40	0.30	5.32	11.53	29.67	8.16
45.00	1.59	1.40	0.30	5.28	11.99	30.19	8.16
50.00	1.58	1.38	0.30	5.21	11.36	30.74	8.17
55.00	1.55	1.36	0.31	5.07	12.47	31.39	8.11
60.00	1.53	1.34	0.31	4.96	12.62	31.90	8.11
65.00	1.56	1.37	0.31	4.98	13.16	32.39	8.11
70.00	1.56	1.37	0.31	4.97	14.39	32.84	8.24

Table A-3 (cont.)

75.00	1.55	1.36	0.32	4.91	13.50	33.67	8.17
80.00	1.51	1.32	0.32	4.74	13.55	34.35	8.29
85.00	1.53	1.33	0.32	4.74	12.92	35.08	8.15
90.00	1.52	1.33	0.32	4.72	13.62	35.88	8.28
95.00	1.52	1.32	0.33	4.63	13.62	36.42	8.32
100.00	1.51	1.32	0.33	4.56	14.36	37.11	8.19
105.00	1.51	1.32	0.33	4.55	14.41	37.79	8.29
110.00	1.50	1.30	0.34	4.48	14.43	38.49	8.29
115.00	1.46	1.27	0.34	4.33	12.97	39.46	8.38
120.00	1.46	1.28	0.34	4.29	14.90	39.93	8.16
125.00	1.49	1.27	0.35	4.30	14.46	40.67	8.26
130.00	1.39	1.20	0.35	3.98	9.19	42.11	8.40
135.00	1.42	1.24	0.35	4.03	13.92	42.25	8.30
140.00	1.45	1.26	0.36	4.07	15.40	42.92	8.18
145.00	1.46	1.26	0.36	4.09	16.25	43.42	8.24
150.00	1.44	1.20	0.36	3.97	13.85	44.82	8.44
155.00	1.40	1.20	0.37	3.80	12.58	45.98	8.48
160.00	1.41	1.22	0.37	3.82	15.33	46.50	8.24
165.00	1.42	1.22	0.37	3.82	16.03	47.15	8.47
170.00	1.40	1.18	0.38	3.71	12.44	48.43	8.55
175.00	1.29	1.17	0.38	3.42	15.04	51.20	0.09
180.00	1.31	1.15	0.39	3.38	13.08	51.79	7.41
185.00	1.32	1.15	0.39	3.35	13.79	53.02	8.34
190.00	1.31	1.14	0.40	3.28	14.01	53.48	8.53
195.00	1.32	1.13	0.40	3.27	14.85	54.44	8.61
200.00	1.34	1.14	0.41	3.26	15.51	55.31	8.55
205.00	1.34	1.13	0.41	3.26	15.64	56.01	8.54
210.00	1.32	1.11	0.42	3.16	15.47	57.08	8.64
215.00	1.32	1.11	0.42	3.16	15.59	56.93	8.55
218.00	1.34	1.12	0.42	3.20	15.51	55.31	8.71

Table A-4 one-circuit condenser with R1234yf

Time [min]	Qcond [kW]	Qevap [kW]	Wcomp [kW]	COP	Ter_o [°C]	Tcr_o [°C]	m [g/s]
5.00	1.00	1.02	0.27	3.75	25.70	29.77	6.86
10.00	1.28	1.21	0.28	4.51	24.31	29.95	8.28
15.00	1.35	1.23	0.29	4.67	23.40	30.18	8.46
20.00	1.39	1.24	0.29	4.78	22.81	30.68	8.60

Table A-4 (cont.)

25.00	1.44	1.26	0.29	4.88	22.47	31.06	8.83
30.00	1.42	1.24	0.30	4.77	22.40	31.62	8.75
35.00	1.43	1.25	0.30	4.78	22.27	32.14	8.87
40.00	1.43	1.25	0.30	4.76	22.12	32.68	8.91
45.00	1.40	1.23	0.30	4.61	22.05	33.30	8.84
50.00	1.41	1.23	0.31	4.59	21.95	33.99	8.91
55.00	1.38	1.21	0.31	4.51	21.87	34.63	8.82
60.00	1.38	1.20	0.31	4.48	21.80	35.28	8.86
65.00	1.38	1.20	0.31	4.44	21.79	35.85	8.87
70.00	1.38	1.20	0.31	4.39	21.81	36.47	8.91
75.00	1.37	1.19	0.31	4.36	21.79	37.11	8.94
80.00	1.39	1.20	0.32	4.34	21.84	37.81	9.06
85.00	1.37	1.19	0.32	4.29	21.85	38.57	9.05
90.00	1.36	1.17	0.32	4.24	21.86	39.12	9.01
95.00	1.34	1.16	0.33	4.13	21.87	39.73	8.96
100.00	1.33	1.15	0.33	4.08	21.88	40.41	8.94
105.00	1.34	1.15	0.33	4.07	21.97	41.15	9.04
110.00	1.34	1.15	0.33	4.05	21.98	41.70	9.08
115.00	1.33	1.14	0.33	3.99	22.03	42.33	9.04
120.00	1.32	1.13	0.34	3.92	22.06	42.92	9.02
125.00	1.31	1.12	0.34	3.88	22.09	43.47	9.00
130.00	1.30	1.11	0.34	3.81	22.18	44.09	8.98
135.00	1.26	1.07	0.34	3.68	22.24	44.86	8.78
140.00	1.27	1.08	0.35	3.69	22.26	45.57	8.94
145.00	1.25	1.06	0.35	3.61	22.30	46.32	8.85
150.00	1.25	1.06	0.35	3.58	22.35	46.86	8.90
155.00	1.25	1.06	0.35	3.56	22.47	47.40	8.95
160.00	1.23	1.04	0.35	3.46	22.48	48.14	8.86
165.00	1.22	1.04	0.36	3.43	22.57	48.87	8.90
170.00	1.22	1.03	0.36	3.39	22.59	49.35	8.91
175.00	1.23	1.04	0.36	3.40	22.72	49.95	9.03
180.00	1.22	1.02	0.36	3.34	22.76	50.70	8.99
185.00	1.22	1.02	0.37	3.31	22.84	51.12	9.06
190.00	1.22	1.02	0.37	3.31	22.84	51.89	9.13
195.00	1.21	1.01	0.38	3.22	22.61	52.70	9.16
200.00	1.20	1.00	0.38	3.17	22.77	53.17	9.14
205.00	1.20	1.00	0.38	3.16	22.82	53.99	9.24

Table A-4 (cont.)

210.00	1.18	0.99	0.38	3.10	22.95	54.60	9.17
215.00	1.19	0.98	0.39	3.06	23.02	55.17	9.21
220.00	1.19	0.98	0.39	3.06	23.07	55.60	9.27
225.00	1.17	0.97	0.39	2.98	23.16	56.52	9.22
230.00	1.17	0.97	0.39	2.98	23.20	56.78	9.24
234.00	1.18	0.97	0.39	3.00	23.17	56.80	9.32